



Nanolaminated $\text{Al}_{100-z}\text{Ni}_z / \text{AlO}_x\text{H}_y$ thin films by hybrid PVD / ALD: An approach towards interface-engineered thin films by dual-route tailoring

Hendrik C. Jansen^{a,b,*}, Amit Sharma^{a,c}, Marcus Hans^d, Jochen M Schneider^d, Jakob Schwiedrzik^{a,e}, Johann Michler^{a,b}, Thomas E.J. Edwards^{a,f,g,*}

^a Laboratory for Mechanics of Materials and Nanostructures, Empa Swiss Federal Laboratories for Material Science and Technology, Feuerwerkerstrasse 39, CH-3602 Thun, Switzerland

^b École Polytechnique Fédérale de Lausanne, Rte Cantonale, CH-1015 Lausanne, Switzerland

^c SwissCluster AG, Bahnhofstrasse 19, CH-3700 Spiez, Switzerland

^d Materials Chemistry, RWTH Aachen University, Kopernikusstraße 10, D-52074 Aachen, Germany

^e Laboratory for High Performance Ceramics, Empa Swiss Federal Laboratories for Material Science and Technology, Überlandstrasse 129, CH-8600 Dübendorf, Switzerland

^f Research Center for Structural Materials, National Institute for Materials Science, 1-2-1 Sengen, Tsukuba, Ibaraki 305-0047, Japan

^g Department of Materials Science, Institute of Pure and Applied Sciences, University of Tsukuba, 1-1-1 Tennodai, Tsukuba, Ibaraki 305-8573, Japan

ARTICLE INFO

Keywords:

Nanolaminated aluminium
Interface-engineering
Hybrid PVD-ALD
Nanoclusters
Crystalline/amorphous interface
Nanoindentation

ABSTRACT

Hybrid physical vapour/atomic layer deposition technology has enabled the formation of nanolaminated $\text{Al}_{100-z}\text{Ni}_z/\text{AlO}_x\text{H}_y$ (bilayer period: 25/1 nm, $z = 0, 2$, and 5 at.%) thin films, introducing a novel interface-engineered design strategy with advanced microstructure control. This leverages dual-route tailoring of nano-crystalline Al through 1) compositional grain boundary engineering ($\text{Al}_{100-z}\text{Ni}_z$) and 2) well-defined crystalline / amorphous interfaces ($\text{Al}_{100-z}\text{Ni}_z/\text{AlO}_x\text{H}_y$). As ambient plasticity is thought to be governed by dislocation interactions with segregation-modified interfaces & lattice, elucidating the collective role of such barriers in strengthening is essential for establishing a robust design framework.

Accordingly, high-resolution analyses by scanning transmission electron microscopy (STEM) and atom probe tomography (APT) established a direct link between enhanced hardness and distinct nanostructural features. The nanolaminated $\text{Al}_{95}\text{Ni}_5 / \text{AlO}_x\text{H}_y$ thin film here exhibits Ni-rich nanoclusters embedded in a sub-10 nm FCC Al matrix and smooth ~ 1 nm amorphous interlayers. Notably, STEM indicated Ni decorating vertical Al grain boundaries, whereas APT reveals these to be distinct Ni-rich nanoclusters. Nanoindentation measurements confirmed hardness of 5.3 GPa for $\text{Al}_{95}\text{Ni}_5/\text{AlO}_x\text{H}_y$ versus 2.7 GPa for $\text{Al}/\text{AlO}_x\text{H}_y$. Calculations showed that comparable strengthening magnitudes originate from both aspects of the dual-route tailored nanostructure: impeding dislocation motion by combined crystalline–amorphous layer confined slip and finely dispersed nanoclusters.

1. Introduction

Aluminium alloys are important engineering materials for a wide range of applications such as the automotive and aerospace sector due to a high specific strength at close-to ambient temperature [1–3]. Strength enhancement of commercial Al alloys with grain sizes in the micrometre range is mainly achieved by a combination of solid-solution strengthening, formation of secondary phases (precipitation strengthening) in the Al matrix or grain refinement [4]. Such distortions of the Al matrix

successfully impede dislocation motion and induce strength values around e.g. 500 MPa reported for Al 6061-T6 [5]. In recent decades, advances in alloy design have included ultrafine-grained (UFG) to nanocrystalline Al alloys (10 nm < grain size < 1000 nm) with strength values beyond 1000 MPa due to increasing grain boundary dislocation pile-up [6–8]. Ma *et al.* [7] reported precipitation-strengthened UFG Al 7075 T6 with up to 734 MPa yield stress and mean Al grain diameter of 245 nm. In a study on UFG AA6061 with mean Al grain size of 30 nm and additionally containing dense Mg-Si clusters, 805 MPa yield stress was

* Corresponding authors at: Laboratory for Mechanics of Materials and Nanostructures, Empa Swiss Federal Laboratories for Material Science and Technology, Feuerwerkerstrasse 39, CH-3602 Thun, Switzerland.

E-mail addresses: hendrik.jansen@empa.ch (H.C. Jansen), thomas.edwards@nims.go.jp (T.E.J. Edwards).

<https://doi.org/10.1016/j.matdes.2026.115580>

Received 21 November 2025; Received in revised form 15 January 2026; Accepted 28 January 2026

Available online 30 January 2026

0264-1275/© 2026 The Author(s). Published by Elsevier Ltd. This is an open access article under the CC BY license (<http://creativecommons.org/licenses/by/4.0/>).

achieved [8]. However, reports on nanostructured Al emphasised strengthening was limited to a maximum service temperature around 200 °C due to catastrophic grain coarsening and precipitation growth limiting the thermal stability [5,6].

To secure mechanical stability at elevated temperatures, nanocrystalline materials require additional kinetic or thermodynamic stabilisation of the grain boundaries [9]. Kinetically, segregations at the grain boundaries might produce stabilisation in the form of physical barriers to grain growth. Thermodynamic stabilisation however, stems from an altered chemical grain boundary state with reduced grain boundary free energy and thus reduced driving force for grain growth [9,10]. Balbus *et al.* [6] reported the formation of structurally disordered interfaces with amorphous character and sub-10 nm grain size in sputter-deposited $\text{Al}_{94.9}\text{Ni}_{3.8}\text{Ce}_{1.3}$. (Scanning) transmission electron microscopy (STEM) and STEM-energy dispersive X-ray spectroscopy (STEM-EDS) investigations showed the formation of Ni- and Ce- agglomerations at grain boundaries compared to both Ni- and Ce-deficient Al grain interiors. The microstructure and amorphous character of Al-Al grain boundaries allowed a room temperature nanoindentation hardness of 5.2 GPa, even after exposure to 250 °C in vacuum for 1 h. Lei *et al.* [11] produced nanocrystalline $\text{Al}_{95.7}\text{Mg}_{2.1}\text{Y}_{2.2}$, $\text{Al}_{95.7}\text{Fe}_{2.2}\text{Y}_{2.1}$, and $\text{Al}_{95.7}\text{Ni}_{2.2}\text{Y}_{2.1}$ alloys by ball milling and subsequent hot-pressing at temperatures of up to 585 °C. The combination of a grain boundary segregating element (Mg, Fe, Ni) [12] and a large atomic radius rare-earth element like Y should result in amorphous segregations at the grain boundaries, similar to designing bulk Al metallic glasses. X-ray diffraction (XRD) confirmed as-milled Al grain sizes in the range of 10 to 19 nm and STEM-EDS the successful formation of amorphous interfaces at the grain boundaries. Notably, dopant enrichment in the amorphous interfaces was derived from STEM-EDS concentration peaks, coinciding with Ga concentration peaks from ion beam preparation. The several nanometres-thick amorphous Mg-Y, Fe-Y, and Ni-Y enrichments at the Al-Al grain boundaries ultimately induced strengthening up to a nanoindentation hardness of 2.8 GPa in the case of Al-Mg-Y, while Al-Fe-Y and Al-Ni-Y had hardnesses of 2.2 and 2.3 GPa, respectively. In other work, XRD and S/TEM were applied to demonstrate Mg-enrichment at the Al-Al grain boundaries of ball-milled $\text{Al}_{93}\text{Mg}_7$ vacuum annealed at 200 °C for 1 h [13]. Micromechanical testing confirmed the following mechanical properties: 4.6 GPa nano-hardness and 865 MPa yield strength from micropillar compression. Hung *et al.* [5] processed $\text{Al}_{100-z}\text{Ce}_z$ and $\text{Al}_{100-z}\text{Co}_z$ ($z = 0.5, 1$, and 3 at.%) alloys by additive manufacturing. At low Co and Ce concentrations of 0.5 at.%, atomic clusters of especially Co atoms were found by STEM, where SAED did not show any phase formation other than FCC Al. Yet, peak hardness values of up to 3.4 GPa in the case of $\text{Al}_{97}\text{Co}_3$ and 3.2 GPa in case of $\text{Al}_{97}\text{Ce}_3$ were successfully linked to the formation of 10 to 30 nm spherical particles of Al-Co and Al-Ce phases. To identify such microstructure features in the near-atomic scale, Guo *et al.* [14] complemented STEM datasets on medium entropy alloy nanolaminates with atom probe tomography (APT). The data unravelled chemical gradients at nano twin boundaries with chemical Cr-Ni-Co variations occurring across a distance of less than 3 nm.

Beyond designing nanocrystalline Al alloys, superior thin film performance through a nanolaminated architecture has been demonstrated in the last decades. In fact, refinement up to only several nm of layer thickness induced significant strengthening towards the theoretical strength limit [15–17]. In several publications, enhanced mechanical properties of nanolaminated thin films were linked to a dislocation impediment by crystalline/crystalline interfaces [18,19], but also crystalline/amorphous interfaces [20–23]. Crystalline/crystalline Al/TiN thin films were found to show nanoindentation hardness of 3.7 GPa in an Al/TiN architecture with 9/1 nm layer thicknesses, whereas increasing the Al and TiN layer thicknesses to 450 and 50 nm, respectively, induced softening as the hardness was reduced to 1.2 GPa. Crystalline/amorphous Cu/CuZr interfaces successfully prevented catastrophic shear banding in CuZr metallic glasses, while maintaining a

total compressive flow stress of 2.6 GPa in a 50/100 nm architecture [20]. Three-dimensional crystalline/amorphous nanoarchitectures in melt-spun Ti-Zr-based alloys have demonstrated yield strengths of approximately 1.8 GPa combined with uniform elongations of about 7.0% [24]. Wei *et al.* [25] reported the formation of ~2 nm amorphous SiOC intergranular films at the boundaries of 13 nm Ni grain boundaries via magnetron co-sputtering of Ni, SiO_2 , and SiC, achieving a room-temperature strength of 2.5 GPa. Similarly, recent studies on magnetron-sputtered Al-Cr alloys with varying Cr content revealed the emergence of combined crystalline/amorphous nanostructures and Cr segregation at crystalline/amorphous interfaces through Cr segregation, leading to yield strengths of up to 1.75 GPa and tensile strains of around 15% [26].

Recent advances in atomic layer deposition (ALD) combined with physical vapour deposition (PVD) offer control over interfacial microstructure and chemistry, enabling the integration of amorphous hard interlayers with exceptional uniformity [22,27,28]. These capabilities are critical for advancing nanolaminated thin films beyond current design and performance limits. Edwards *et al.* [22,27] reported enhanced strength in crystalline/amorphous Al/ Al_2O_3 with bilayer period of 250/(1–10) nm processed by hybrid PVD/ALD. Accordingly, the Al/ Al_2O_3 interfaces showed high strength, being promising for enhanced interface bonding and multilayer stability, and prevented crack formation as observed at weaker CrAlSiN/ Al_2O_3 interfaces in another work [29]. The ultra-thin amorphous Al_2O_3 interlayers triggered Al grain renucleation, while micropillar compression determined a yield stress of approximately 532 MPa – 107 MPa more than the pure PVD reference sample. Notably, the Al grain renucleation was found to occur even when pulsing only one full ALD cycle, whereas thermal stability could be maintained with minimum interlayer thickness of 1 nm. Most recently, Baral *et al.* [23] showed enhanced mechanical properties of nanolaminated Al/ Al_2O_3 deposited by hybrid (reactive) magnetron sputtering with varying layer thicknesses. Applying nanoindentation, a nanolaminated film with 44/5 nm bilayer period exhibited > 2 GPa nanoindentation hardness. Here, reference is only made to the lowest volume fraction of Al_2O_3 interlayers in the thin film stack for comparability as an increasing Al_2O_3 volume fraction significantly enhances the indentation hardness (44/5 nm Al/ Al_2O_3 : $f_{\text{Al}_2\text{O}_3} = 10.2\%$). Excellent mechanical response was derived from ductile FCC Al and hard amorphous Al_2O_3 layers, where constrained plasticity in Al enhances strength, while the amorphous Al_2O_3 suppresses shear banding and resists crack propagation.

Here, we allow to go one step further in the design of nanocrystalline interface-engineered Al alloys by combining magnetron co-sputtering (PVD), and ALD, thus dual-route tailoring. This dual-route tailoring approach not only aims to improve ambient strength, but has a future vision of enabling good high temperature strength retention through advanced grain size control in nanocrystalline metals. Indeed, PVD complexions could stabilise in-plane grains, whilst the nanolayer thicknesses of ALD interlayers achieved through their self-limiting surface reactions is expected to provide even greater control of out-of-plane dimensions—together forming a coupled thermokinetic pathway that effectively stabilises the nanocomposite structure.

The henceforth derived vision for the $\text{Al}_{100-z}\text{Ni}_z/\text{AlO}_x\text{H}_y$ thin film design and processing is illustrated in Fig. 1. Ni was chosen as dopant in the Al layer based on the work of Murdoch and Schuh [12] as well as Wagih *et al.* [30] since it has been predicted that Ni is a viable candidate for grain boundary segregation in Al, following the promising pathway of complexion-engineered nanocrystalline metals [31–33]. The low amount of 5 at.% will then allow a direct comparison to previously reported promising compositionally-designed Al-Zr, Al-Mg, Al-Ti, Al-W, Al-Mo, Al-Ag, Al-Cr, Al-Fe, Al-Co, and Al-Ni alloys with only 5–6 at.% of solute addition [34]. Moreover, the low amount of dopant in the Al matrix actively avoids phase separation to Al_3Ni and Al, which is predicted by the stability phase diagram [35] and observed experimentally already for 5.7 at.% Ni at room-temperature [36]. Notably, interface

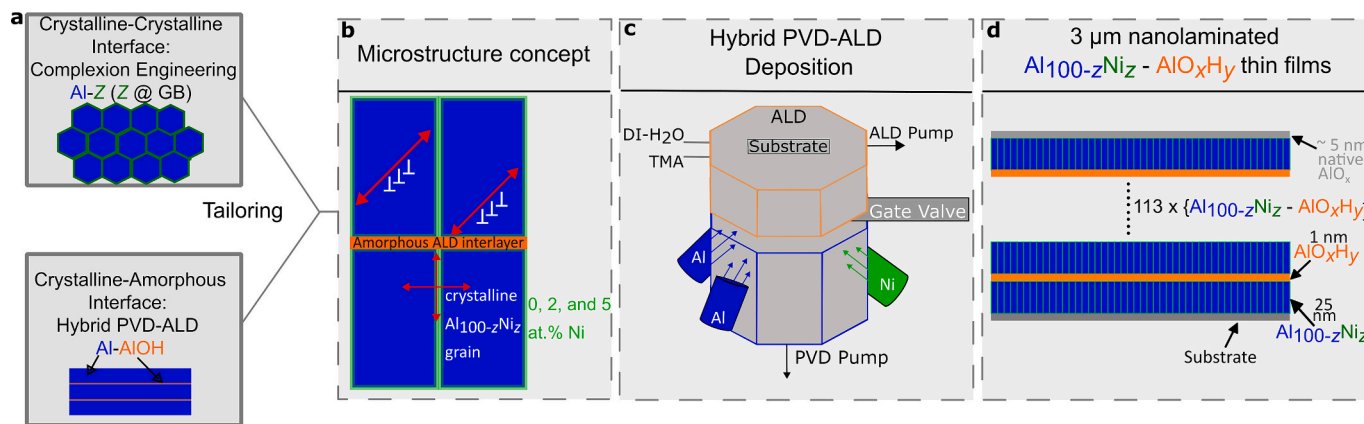


Fig. 1. Scope of the current study: (a) Principle of crystalline-crystalline tailoring by Al-Ni co-deposition and crystalline-amorphous tailoring by Al / AlO_xH_y nanolaminating resulting in (b) the concept microstructure of crystalline $\text{Al}_{100-z}\text{Ni}_z$ grains with thin amorphous ALD AlO_xH_y interlayers interfering with both dislocation motion and thermally activated grain growth, (c) sketch of deposition set-up including positioning of ALD precursor inlets, exhaust and PVD magnetrons, as well as (d) the full 3 μm thin film stack consisting of 114 bilayer periods of 25 / 1 nm for $\text{Al}_{100-z}\text{Ni}_z$ / AlO_xH_y .

segregation is more desirable than matrix segregation due to reduced interfacial energy and thus, stabilised microstructure, whereas segregation within the matrix often leads to precipitation or embrittlement without providing such interfacial stabilization [37]. Despite other binary and ternary Al-X-Y systems with e.g., X = Mg and Y = Ce being already reported to show segregation to Al grain boundaries [6,12,13], alloying Mg or Ce to the Al layer of Al / AlO_xH_y thin films is undesirable here due to its destabilising effect on the amorphous AlO_xH_y interlayers: the Ellingham diagram predicts MgO_x and CeO_x to be more stable than Al_2O_3 (AlO_xH_y) interlayers due to lower enthalpy of formation [38].

Hence, we aim to engineer hierarchical dimensional control, with one-dimensional out-of-plane tuning through nanolaminating, and two- and three-dimensional in-plane control via nanocrystalline grain arrangement and interface complexity, Fig. 1. The tailored $\text{Al}_{100-z}\text{Ni}_z$ / AlO_xH_y thin films are hypothesised to inhibit dislocation and grain boundary motion both in- and out-of-plane as illustrated in Fig. 1b to achieve enhanced mechanical properties and thermal stability. The processing strategy then consists of loops of PVD – ALD to repeat the basic bi-layer building block 114 times to obtain roughly 3 μm nanolaminated thin films, as depicted in Fig. 1d. Here, we aim to understand to what extent such a microstructure causes improved mechanical properties, and comprehend the underlying mechanisms through a detailed analysis of the microstructure and hence strength modelling. A full exploration of thermal stability will be the topic of future work.

2. Materials and methods

2.1. Materials fabrication

The nanolaminated $\text{Al}_{100-z}\text{Ni}_z$ / AlO_xH_y thin films were deposited by means of combined PVD and ALD in a SwissCluster AG SC-1 hybrid deposition chamber. The two distinct deposition processes are linked in a fully automated manner where magnetron sputtering occurs with opened chamber-separating gate valve allowing sputtering “through” the gate valve, whereas ALD layers are processed with the gate valve closed. The crystalline $\text{Al}_{100-z}\text{Ni}_z$ layers were sputtered from two 2” Al targets (99.999% purity, HMW Hauner AG) and additionally one 2” Ni (99.99+ % purity, HMW Hauner AG) target for Ni-doping. Magnetron sputtering was carried out at 280 mA direct current on each Al target as well as high power impulse magnetron sputtering (HiPIMS) of the Ni target at 15 and 33 mA average to achieve global Ni concentrations of 2 and 5 at.%, respectively, in the metallic layers. HiPIMS was performed at 500 Hz frequency, 20 μs pulsing, and 15 A peak current. The hence-achieved sputter deposition rate was roughly 0.08 nm s^{-1} . The base pressure of the chamber prior to each PVD cycle was below 9×10^{-7}

mbar, whereas the deposition pressure was kept constant at 5×10^{-3} mbar with an Ar flow of 10 sccm. Four-inch Si + 80 nm amorphous Si_3N_4 substrates (MicroChemicals GmbH) were chosen for each deposition. To avoid excessive grain growth of the nanocrystalline $\text{Al}_{100-z}\text{Ni}_z$ grains during deposition, no substrate or chamber heating was applied, and the temperature of the substrate stage was 298 K. The substrate-to-targets distance was 270 mm.

ALD of AlO_xH_y was carried out by alternating half-cycles of $(\text{CH}_3)_3\text{Al}$ (TMA) and DI H_2O at room temperature. No heating was applied similarly to the PVD process to not induce growth of the nanocrystalline $\text{Al}_{100-z}\text{Ni}_z$ grains, although this results in significant hydrogen incorporation of up to 20 at.% in the ALD layer from residual H of the DI H_2O precursor [39,40]. Pulse and purge conditions for TMA of 200 ms at 250 sccm Ar, and 20000 ms at 500 sccm Ar, respectively, were used, whereas DI H_2O was processed with 150 ms at 250 sccm, and 20000 ms at 500 sccm Ar, respectively. The ALD deposition pressure was maintained in the 10^{-1} mbar range, where 6 cycles result in deposition of roughly 1 nm continuous and amorphous AlO_xH_y .

2.2. Materials characterisation

Phase formation of every sample condition was analysed by XRD using a Bruker D8 Discovery in Bragg-Brentano geometry. The instrument broadening was corrected by measuring a LaB_6 standard at $2\theta = 40^\circ$. Due to the small feature sizes in the nanolaminated $\text{Al}_{100-z}\text{Ni}_z$ / AlO_xH_y thin films, a combination of TEM and APT is applied to allow high-resolution microscopy beyond the 2D spatial resolution in the TEM projection plane around $\leq 1 \text{ nm}$. In fact, certain microstructure features in that 3D size range $< 1 \text{ nm}^3$ are expected to significantly influence the mechanical properties and thermal stability of these interface-engineered materials [11,13,33]. TEM samples were prepared by a Thermo Fisher Scientific (TFS) Helios 5 Hydra DualBeam plasma Focused Ion Beam – Scanning Electron Microscope (PFIB-SEM) equipped for Xe^+ milling, following the procedure for site-specific TEM specimens in our previous work to avoid Ga-induced misinterpretation [41]. TEM was conducted on a TFS aberration corrected (probe) Themis 200 G3 operated at 200 kV to capture grain morphology, and identify local crystallography and chemistry. Analysis of STEM images, fast Fourier transformation (FFT) patterns, and selected area electron diffraction (SAED) patterns was conducted using the CrystBox software [42], whilst STEM-EDX data was analysed using TFS proprietary Velox software.

Atom probe specimens were prepared using PFIB as well. A protection layer, employing Pt and C precursors (99 and 1%, respectively, in TFS proprietary flow control), was deposited using ions at 12 kV energy,

while milling operations were conducted at 30 kV. Plan-view lift-outs were performed (see supplementary material of [43]) in order to align the Al / AlO_xH_y interfaces parallel to the specimen shank. Sharpening was carried out at 12 kV with the final polish at 5 kV. APT was performed in a CAMECA local electrode atom probe (LEAP) 4000X HR. Field evaporation was assisted by voltage pulsing with 20% pulse fraction, 100 kHz pulse frequency, 60 K base temperature and 0.5% detection rate. At least 50 million ions were acquired and data reconstruction was performed with CAMECA AP Suite 6.1, employing the shank angle protocol. The reconstructions were tuned with respect to the bilayer thicknesses of 25 / 1 nm. Visualisation of the interfaces was realised with 10 nm thick slices of the reconstructions. H was included in the ranging of mass spectra and the content can be understood as an upper boundary value due to the likely contribution of residual gas from the analysis chamber.

Evaluation of mechanical properties by nanoindentation was performed on a Zwick Roell nanoindenter system (ZHN Nanoindenter, ZwickRoell GmbH & Co. KG, Ulm, Germany) equipped with a Berkovich diamond tip. A total of 25 indents were collected per sample condition. The indentation experiments were conducted using a quasi-static displacement-controlled loading protocol with maximum indentation depth of 1 μm . The hardness values were derived from a plateau region between 100 and 300 nm indentation depth as proposed by Fischer-Cripps [44]. Measurement uncertainties account for the hardness variation over a depth range of 100–300 nm and the statistical uncertainty derived from 25 individual indents. Representative depth-resolved hardness for each sample condition is provided in the Supplementary Material.

3. Results and discussion

3.1. Phase formation

Fig. 2 displays an overview of the three different as-deposited $\text{Al}_{100-z}\text{Ni}_z / \text{AlO}_x\text{H}_y$ (25 / 1 nm, bilayer period in the following not mentioned; $z = 0, 2$, and 5 at.%) thin films in terms of high angle annular dark field (HAADF)-STEM images of several tens of bilayers and single Al grains in the middle of the film stack. It is noted that throughout this article, the three Al / AlO_xH_y , $\text{Al}_{98}\text{Ni}_2 / \text{AlO}_x\text{H}_y$, and $\text{Al}_{95}\text{Ni}_5 / \text{AlO}_x\text{H}_y$ will be depicted in Figures with dark red-, dark purple-, and pink-colored frames, respectively. Additionally, information regarding Al, Ni, and O composition are visualised consistently through the colour code blue, green, and orange, respectively.

The HAADF-STEM images in Fig. 2 confirm the nanolaminated nature of $\text{Al}_{100-z}\text{Ni}_z / \text{AlO}_x\text{H}_y$ thin films with homogenous and constant bilayer period of $25 (\pm 2.2) / 1 (\pm 0.2)$ nm. It is emphasised that precise measurement of the 1 nm AlO_xH_y interlayers is impeded by the 1 nm layer thickness versus roughly 50 to 70 nm TEM lamella thickness, and the imperfect flatness of the metallic layers onto which the ALD layer conformally grows, and consequent electron scattering events, making the AlO_xH_y often appear broader. There is a reduction in surface roughness of the crystalline $\text{Al}_{100-z}\text{Ni}_z$ layers compared to the pure Al layers, causing the Ni-doped nanolaminated $\text{Al}_{98}\text{Ni}_2 / \text{AlO}_x\text{H}_y$ and $\text{Al}_{95}\text{Ni}_5 / \text{AlO}_x\text{H}_y$ thin films to contain smoother crystalline / amorphous interfaces. Secondly, significant differences in the in-plane FCC $\text{Al}_{100-z}\text{Ni}_z$ grain size are visible, as measured from dark field (DF)-TEM images. Representative DF-TEM images of each thin film with objective aperture on (111) and (200) FCC Al diffractions as well as corresponding layer thickness and grain size distributions can be found in the supplementary material. At least 70 grains were measured per sample and the range corresponds to the standard deviation of measured values. Hence-derived layer thicknesses are 25.0 ± 2.5 nm, 24.3 ± 1.3 nm, and 24.8 ± 1.1 nm for Al / AlO_xH_y , $\text{Al}_{98}\text{Ni}_2 / \text{AlO}_x\text{H}_y$, and $\text{Al}_{95}\text{Ni}_5 / \text{AlO}_x\text{H}_y$, respectively. Since the layer thickness variations are within the measurement uncertainty, the three architectures are collectively denoted as 25 / 1 nm throughout this work for simplicity. The Al / AlO_xH_y in Fig. 2a

shows a lateral FCC Al grain size of 28.0 ± 7.6 nm, while Ni-doping of 2 and 5 at.% to the crystalline Al-layer results in lateral grain size refinement to 12.5 ± 4.2 nm and 8.7 ± 2.6 nm, respectively. Thus, up to 5 at.% Ni in the crystalline Al matrix reduces the lateral grain size by approximately 70%.

Additionally, HR-STEM imaging, and subsequent reduced-area FFT patterns of grains viewed along [110] poles, were conducted to approach the local arrangement of Al, Ni, and O atoms. Results in Fig. 2b, d, and f confirm the crystalline nature of FCC Al(-Ni) grains, while the lack of periodicity from 1 nm AlO_xH_y ALD layers hints towards an amorphous atomic arrangement. Furthermore, HR-TEM imaging, validated through FFT analysis, was performed to confirm the amorphous nature of the interlayer. Fig. 2g shows an HR-TEM image of 2 bilayer periods with reduced area FFT insets for the interlayer (Fig. 2h) and an Al-Ni grain (Fig. 2i). Distinct diffraction spots in the FFT in Fig. 2i, in contrast to the absence of such features for the interlayer in Fig. 2h, confirm the true AlO_xH_y amorphous nature.

Additionally, there is no immediate evidence for Ni-decoration – neither at vertical Al-Al grain boundaries, nor at crystalline / amorphous interfaces.

Results on phase formation from both XRD and SAED are displayed in Fig. 3. Bragg-Brentano XRD in Fig. 3a confirms that Ni-alloying of the crystalline Al matrix does not induce phase formation other than crystalline FCC Al. In fact, all as-deposited conditions show a strong (111) FCC Al texture with peak broadening when the layers were Ni-doped, whereas the (200) Al reflection at $2\theta = 44.7^\circ$ is significantly reduced in intensity through Ni-doping of the Al matrix. Thus, based on XRD data a metastable Al-Ni solid solution is formed, while the thermodynamic equilibrium phase diagram predicts the formation of FCC Al and orthorhombic Al_3Ni [35]. The peak at $2\theta = 34.8^\circ$ in the diffractograms stems from $\text{Cu K } \beta$ (111) FCC Al rather than crystalline orthorhombic $\kappa\text{-Al}_2\text{O}_3$. In contrast to the crystalline Al phase, the AlO_xH_y interlayers are X-ray amorphous in all three as-deposited conditions. To complement the dataset from XRD, SAED with an aperture size of roughly 580 nm diameter, covering approximately 20 bilayers, was performed. SAED patterns in Fig. 3b–d confirm strongest diffraction arising from (111) and (200) FCC Al planes in all conditions with no other phase visible. In the pure Al layers, discrete diffraction spots of several FCC Al planes originate from a more randomly oriented distribution of larger grain sizes, whereas more continuous rings in the Ni-doped thin films are due to a greater number of differentially diffracting volumes, i.e. a refined grain size, with additionally more pronounced (111) FCC Al out-of-plane texture.

The STEM images reveal that Ni addition to the FCC Al layers induces lateral grain size refinement and interface smoothening. Zhang *et al.* [45] showed that 6 at.% Ni in FCC Al, synthesised by co-sputtering, induced grain refinement from approximately 450 nm to less than 10 nm, which is consistent in trend and magnitude with the results here. These observations are in agreement with the theory of co-sputtering from several targets and the subsequent effect of Ni in solute drag [46]. Notably, the Ni adatoms from HiPIMS will impede FCC Al grain growth and grain coalescence, and boost renucleation. Strong renucleation tendencies of FCC Al grains compared to conventional magnetron-sputtered metals [47] can already be observed in undoped Al / AlO_xH_y (see Fig. 2a). Yet, even smoother crystalline layers are observed by Ni-doping – resulting in more uniform AlO_xH_y interlayers in Fig. 2c and e. Roughness average (Ra) analysis was conducted to determine the arithmetic averages of surface roughness of crystalline / amorphous interfaces based on STEM images. The processed images can be found in the supplementary material. Notably, Ra values of > 3 , 0.8 ± 0.1 , and 0.5 ± 0.1 nm can be derived from measurement of seven interfaces in each case of Al, $\text{Al}_{98}\text{Ni}_2$, and $\text{Al}_{95}\text{Ni}_5$, respectively. Coherent analysis for the pure Al layers is significantly impeded by layer overlapping in STEM images. However, Ni alloying of the FCC Al layers results in significant layer smoothening by roughly 80% reduced surface roughness in case of $\text{Al}_{95}\text{Ni}_5$.

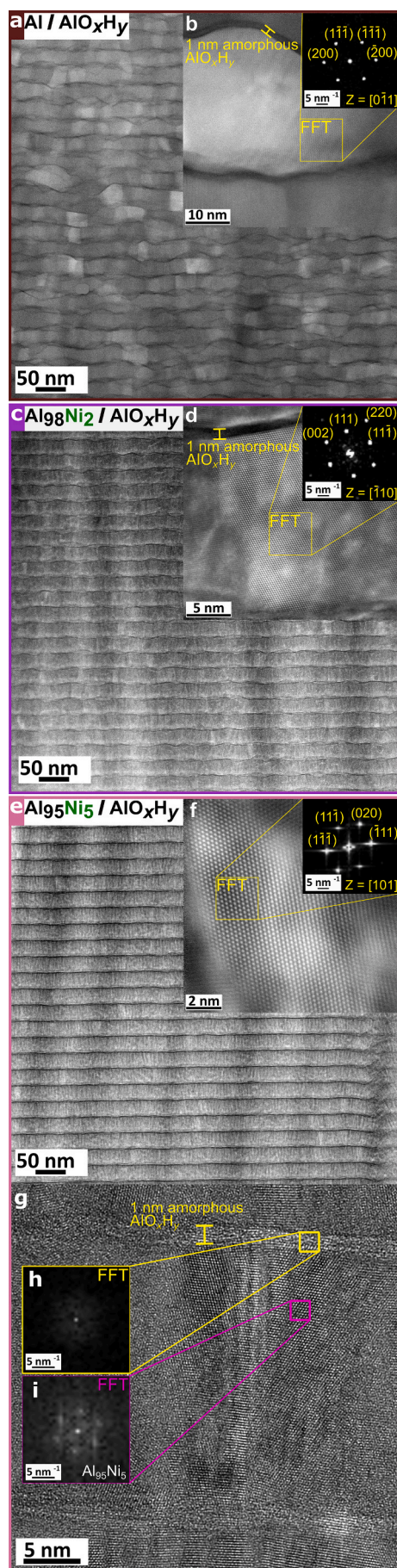


Fig. 2. Overview of S/TEM investigation: HAADF-STEM images of several tens of bilayers (a) Al / AlO_xH_y, (c) Al₉₈Ni₂ / AlO_xH_y, and (e) Al₉₅Ni₅ / AlO_xH_y; HR-STEM images including reduced area FFT from FCC Al grains in (b) Al / AlO_xH_y, (d) Al₉₈Ni₂ / AlO_xH_y, and (f) Al₉₅Ni₅ / AlO_xH_y; as well as (g) HR-TEM of 2 bilayer periods Al₉₅Ni₅ / AlO_xH_y with reduced area FFT inset for (h) AlO_xH_y and (i) Al₉₅Ni₅.

XRD, SAED, as well as FFT of HR-STEM images were performed to analyse the phase formation and effect of Ni on the crystallinity of the FCC (Al). We first focus on the XRD (111) FCC Al peak in Fig. 3a. While the presence of 2 at.% does not noticeably alter the lattice parameter compared to the unalloyed Al layers, 5 at.% of Ni in Al does induce a small peak shift. In fact, the (111) peak positions can be found around $38.480 \pm 0.001^\circ$, $38.487 \pm 0.001^\circ$, and $38.458 \pm 0.004^\circ$ for 0, 2, and 5 at.% Ni, respectively. Applying Bragg's law with 0.1542 nm X-ray wavelength from CuK α radiation, the FCC Al lattice parameters can be derived as 4.047, 4.047, and 4.050 Å, respectively. Thus, the evolution of XRD data is not in agreement with Vegard's rule for Al, Al₉₈Ni₂, and Al₉₅Ni₅ solid solutions, as one would expect lattice parameters of 4.040, 4.029, and 4.012 Å, respectively. While Pun *et al.* [13] were able to track Al lattice constant rise, upon alloying up to 7 at.% Mg to nanocrystalline Al, and subsequently derived grain boundary enrichment with Mg, no such observation can be made here. It is emphasised that XRD should elucidate diffraction information more clearly here than electron diffraction due to the lack of dynamic scattering events [48]. Therefore, no clear trend of reduced lattice plane spacing from Ni-addition and formation of an Al-Ni solid solution can be derived, suggesting phase formation deviating from solely Al-Ni solid solution.

3.2. Elemental distribution and chemical phase mapping

The local chemistry of multiple representative 25 / 1 nm bilayer periods Al_{100-z}Ni_z / AlO_xH_y was mapped by STEM-EDS, in Fig. 4. The HAADF- and Al-O-yield in Al / AlO_xH_y, Al₉₈Ni₂ / AlO_xH_y, and Al₉₅Ni₅ / AlO_xH_y are depicted in Fig. 4a–c and Fig. 4d–f, respectively. In-plane chemical quantification in Fig. 4j–l was derived from measuring four Al(–Ni) layers per sample with each ca. 3000 nm² area (150 x 20 nm). Out-of-plane chemical quantification visualised in Fig. 4d–f stems from analysing vertically along the full STEM-EDS scans and thus, around 30000 nm² scan area (150 x 200 nm). Fig. 4g shows a representative Xe-yield map emphasizing the random distribution and overall negligible Xe-content, while Fig. 4h and i show Ni-yield for 2Ni- and 5Ni-doped Al layers. As above, the HAADF-STEM images in Fig. 4a–c emphasise the smoothening effect of the crystalline-amorphous interface upon alloying 2 and 5 at.% Ni to the crystalline Al layers. Considering the lateral Al grain size given in section 3.1 from DF-TEM, Fig. 4h and i further confirm the lateral grain size refinement upon Ni-addition by the regularity of the vertical HAADF features (vertical bright lines) coinciding with the vertical Al-Al grain boundaries in Al₉₈Ni₂ / AlO_xH_y and Al₉₅Ni₅ / AlO_xH_y that define the lateral Al grain size. The more distinct crystalline-amorphous interfaces upon Ni-addition are additionally confirmed through a clear Al-rich and O-deficient EDS mapping as visualised in Fig. 4d–f. Differences in the Ni-yield are depicted in Fig. 4h and i: in fact, in the case of Al₉₈Ni₂ / AlO_xH_y, Ni appears homogeneously distributed in the crystalline layers with Ni-enrichment in the vicinity of amorphous AlO_xH_y. However, for Al₉₅Ni₅ / AlO_xH_y, there seems to be an additional enrichment of Ni at vertical Al-Al grain boundaries.

Quantitatively, the analysis of the local chemistry of Al layers in the Al / AlO_xH_y architecture indicates 2.8 ± 0.8 at.% O-containing homogeneous Al layers, whereas the amorphous AlO_xH_y interlayers can be quantified as Al_{91.2±1}O_{8.8±1.1}. The accurate quantification of the amorphous interlayers is however hampered by severe overlapping and thickness influence of the TEM specimen and interface roughness as visualised in Fig. 4a and d and is therefore treated approximately as a

(caption on next column)

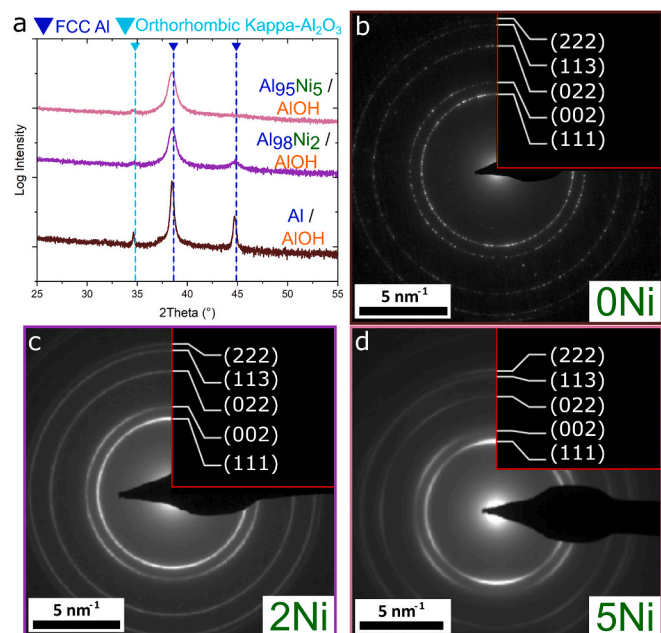


Fig. 3. Diffraction results from nanolaminated $\text{Al}_{100-x}\text{Ni}_x / \text{AlO}_x\text{H}_y$ (25 / 1 nm) thin films: (a) Bragg-Brentano X-ray diffractograms as well as SAED patterns of (b) Al / AlO_xH_y , (c) $\text{Al}_{98}\text{Ni}_2 / \text{AlO}_x\text{H}_y$, and (d) $\text{Al}_{95}\text{Ni}_5 / \text{AlO}_x\text{H}_y$.

lower bound for oxygen content in the AlO_xH_y layers. When aiming for 2 at.% Ni alloying of the crystalline Al layer, STEM-EDS confirms a homogenous chemistry of 2.2 ± 0.2 at.% Ni, 93.1 ± 0.5 at.% Al, and 4.7 ± 0.4 at.% O, while the chemistry of the smoother amorphous interlayers is measured to be $\text{Al}_{77.2 \pm 0.6}\text{Ni}_{2.8 \pm 0.1}\text{O}_{20 \pm 0.6}$. The nominal 5 at.% Ni condition shows 4.9 ± 1 at.% O-containing $\text{Al}_{89.2 \pm 1.3}\text{Ni}_{5.9 \pm 0.9}$ layers with $\text{Al}_{77.7 \pm 0.7}\text{Ni}_{6.5 \pm 0.2}\text{O}_{15.8 \pm 0.8}$ interlayers. Quantitative analysis for the $\text{Al}_{100-x}\text{Ni}_x$ chemistries is derived from the representative EDS linescans in Fig. 4j–l, whereas AlO_xH_y chemistries are derived from the EDS linescans visible in Fig. 4d–f. Overall, the EDS linescans confirm both Ni-doped systems show Ni-diffusion from the crystalline Al–Ni layer to the amorphous AlO_xH_y interlayers. Hydrogen quantification is not considered due to insensitivity of STEM-EDS and a detailed analysis using APT is provided in section 3.3.

For better visualisation of the local Ni distribution, Fig. 5 presents a more magnified STEM-EDS-mapping of the $\text{Al}_{95}\text{Ni}_5 / \text{AlO}_x\text{H}_y$ thin film. Fig. 5a and b show respective HAADF- and Ni-yield similar to the illustration in Fig. 4h and i. One can clearly identify preferential Ni-agglomeration in the vicinity of vertical Al–Al grain boundaries and adjacent to the amorphous AlO_xH_y interlayers. Further evidence for this conformity is provided upon comparing the HAADF and Ni net atomic fraction of the scan. In fact, both the HAADF- and Ni-atomic fraction peak exactly in the same locations in an in-plane line scan over a few FCC Al grains, as illustrated in Fig. 5c. Moreover, Fig. 5d confirms Ni agglomeration in the vicinity of the amorphous AlO_xH_y interlayers upon scanning over three bilayer periods. The line profile shows strongest Ni-intensity coinciding with enhanced brightness around the AlO_xH_y interlayers. In fact, the maximum atomic fraction of Ni shows a 5.3 ± 1.6 nm offset to the HAADF intensity peaks in Fig. 5d. Yet, the analysis of exact peak offset is hampered by any imperfections of alignment of TEM-specimen and electron beam: a slightly inclined specimen angle makes chemical quantification of thin planar features challenging. While STEM-EDS demonstrates preferential Ni segregation at Al grain boundaries, the 3D nanoscale resolution of APT enables a more rigorous quantitative treatment, which is presented in the following section.

There are no existing studies on the STEM-EDS quantification of ~ 1 nm amorphous AlO_xH_y interlayers embedded in a nanolaminated metallic architecture. However, the results reported here clearly link Al-

rich and O-deficient layers to the crystalline FCC Al(–Ni) as well as Al-deficient and O-rich layers to the ALD-deposited amorphous AlO_xH_y , respectively. The Al/O ratios, measured by STEM-EDS, strongly differ between the thin films here. For Al / AlO_xH_y , the high interface roughness further impedes the quantification of Al/O ratio, which is significantly higher than the values measured for the Ni-containing thin films with 10 versus 4 (2 at.% Ni) and 5 (5 at.% Ni), respectively. Shi *et al.* [49] reported Al/O ratios of around 0.2 by SEM-EDS for amorphous Al_2O_3 deposited by TMA and DI H_2O at 200 °C with at least 100 ALD cycles (min. 11.62 nm). Thus, STEM-EDS derived chemical quantification of AlO_xH_y here is taken into account solely qualitatively, further impeded by room temperature ALD being expected to modify the Al/O ratio by H and O enrichment towards a larger H/Al ratio [39,40]. Nevertheless, STEM-EDS additionally confirmed Ni agglomeration in the amorphous AlO_xH_y , visible especially in the Ni-yield of the $\text{Al}_{98}\text{Ni}_2 / \text{AlO}_x\text{H}_y$ in Fig. 4e. The Ellingham diagram predicts NiO_x to be much less favourable to form than AlO_x [38]. We are expecting neither NiO_x nor any ternary Al–Ni–O phases to form. In fact, the thermodynamically stable Al–Ni–O phases Al_2NiO_4 , $\text{Al}_5(\text{NiO}_4)_3$, $\text{Al}_4(\text{NiO}_4)_3$, $\text{Al}_2\text{Ni}_2\text{O}_7$, AlNiO_3 [50,51] exceed global Ni-contents here explicitly as the formation of e.g., Al_2NiO_4 requires 14.3 at.% of Ni locally, which is not in the range of Ni detected by STEM-EDS. However, Fig. 4 and Fig. 5 correlate higher z contrast at vertical Al–Al grain boundaries with preferential Ni agglomeration in the vicinity of vertical Al–Al grain boundaries and amorphous AlO_xH_y interlayers. These findings support the idea of Ni segregation tendencies at Al–Al grain boundaries [12]. Similarly, Balbus *et al.* [6] reported amorphous grain boundary interfaces in sputter-deposited $\text{Al}_{94.9}\text{Ni}_{3.8}\text{Ce}_{1.3}$ thin films. The authors argued that there were significant chemical variations from STEM-EDS mapping for Ni and Ce enrichments of 3.5 to 4.1 at.% and 1.32–1.35 at.%, respectively. A similar brightness-contrast was observed between the FCC Al grains and adjacent grain boundary areas in HAADF-STEM imaging. Here, Ni-yield in the crystalline Al layer of $\text{Al}_{95}\text{Ni}_5 / \text{AlO}_x\text{H}_y$ ranges from lowest 5 at.% in the FCC Al grains to 6.8 at.% in the vicinity of Al grain boundaries. Lei *et al.* [11] suggested dopant agglomeration at grain boundaries in ball-milled $\text{Al}_{95.7}\text{Mg}_{2.1}\text{Y}_{2.2}$, $\text{Al}_{95.7}\text{Fe}_{2.2}\text{Y}_{2.1}$, and $\text{Al}_{95.7}\text{Ni}_{2.2}\text{Y}_{2.1}$, while also an elevated Ga concentration was observed. However, in a previous study we postulated phase transformation by Ga^+ -FIB preparation in these $\text{Al}_{95}\text{Ni}_5 / \text{AlO}_x\text{H}_y$ thin films towards FCC Al and orthorhombic Al_3Ni Dopant fluctuations were also observed in ball-milled $\text{Al}_{93}\text{Mg}_7$ samples with 24 nm grain size [13]. Notably, annealing at 200 °C triggered Mg diffusion towards the grain boundaries with fluctuations around 5 to 10 at.% Mg as shown by STEM-EDS; the dopant peak at the Al–Al grain boundaries is similar to the fluctuations in Ni-yield observed here. In a study on additively manufactured $\text{Al}_{99.5}\text{Co}_{0.5}$, STEM-EDS was applied to show atomic clusters of Co atoms, while no other phases than FCC Al were detected with SAED [5]. Only with globally more than 0.5 at.% Co was the secondary phase formation of Al_9Co_2 detectable. It is evident that STEM-EDS is often used to analyse the chemistry of nanocrystalline Al alloys. Yet, the feature size and reactivity of Al with Ga [41,52] can be expected to significantly impede the analysis. [41]. Thus, it remains unclear, whether amorphous Mg–Y, Fe–Y, and Ni–Y complexions could indeed be caused by active microstructure modification through Ga^+ bombardment during TEM sample preparation. Additionally, the novel microstructure here requires light element characterisation including e.g. O and H – not consistently feasible with STEM-EDS [39,40]. To that extent, 3D chemical mapping by APT from Xe^+ -pFIB prepared specimens was used for identification of nm-size features and interface decorations.

3.3. 3D chemical mapping

APT data of $\text{Al}_{98}\text{Ni}_2 / \text{AlO}_x\text{H}_y$ and $\text{Al}_{95}\text{Ni}_5 / \text{AlO}_x\text{H}_y$ thin films are displayed in Fig. 6 and Fig. 7, respectively. Note that a rotated cross-section lift-out was chosen as specimen preparation method, illustrating three bilayer periods of the nanolaminates in 90° rotation in

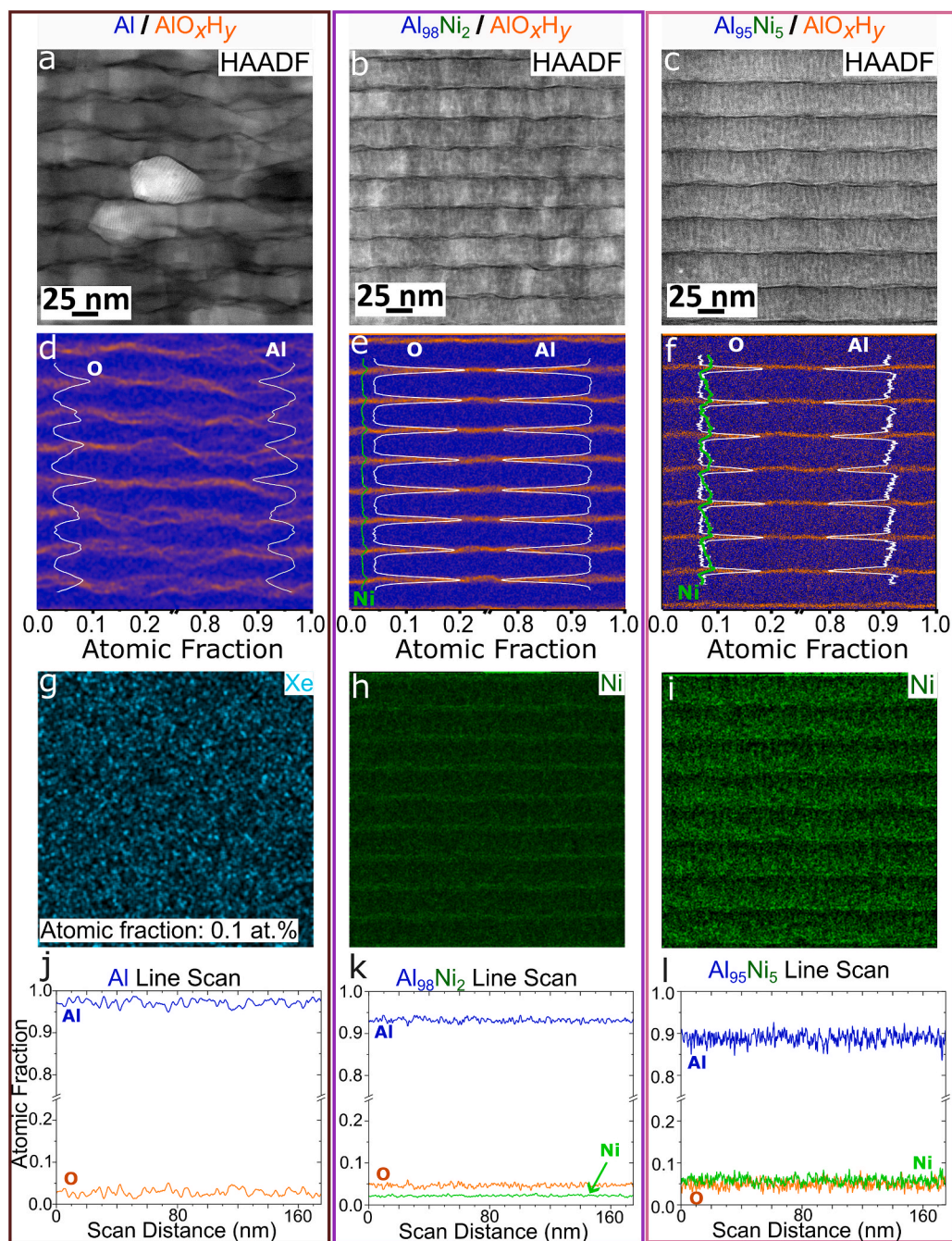
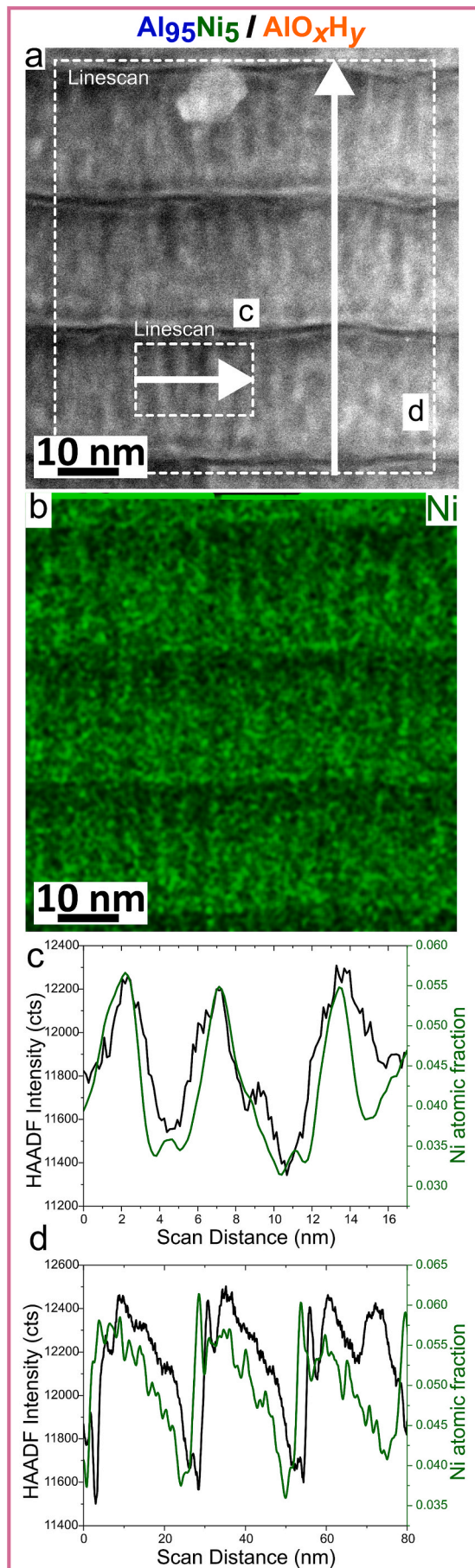


Fig. 4. Chemical mapping of $\text{Al}_{100-z}\text{Ni}_z / \text{AlO}_x\text{H}_y$ bilayer systems by STEM-EDS. HAADF-yield of (a) $\text{Al} / \text{AlO}_x\text{H}_y$, (b) $\text{Al}_{98}\text{Ni}_2 / \text{AlO}_x\text{H}_y$, and (c) $\text{Al}_{95}\text{Ni}_5 / \text{AlO}_x\text{H}_y$; Al-O-yield and out-of-plane EDS line scan for (d) $\text{Al} / \text{AlO}_x\text{H}_y$, (e) $\text{Al}_{98}\text{Ni}_2 / \text{AlO}_x\text{H}_y$, and (f) $\text{Al}_{95}\text{Ni}_5 / \text{AlO}_x\text{H}_y$; (g) representative Xe-yield from PFIB preparation; Ni-yield of (h) $\text{Al}_{98}\text{Ni}_2 / \text{AlO}_x\text{H}_y$ and (i) $\text{Al}_{95}\text{Ni}_5 / \text{AlO}_x\text{H}_y$; in-plane EDS line scan of (j) $\text{Al} / \text{AlO}_x\text{H}_y$, (k) $\text{Al}_{98}\text{Ni}_2 / \text{AlO}_x\text{H}_y$, and (l) $\text{Al}_{95}\text{Ni}_5 / \text{AlO}_x\text{H}_y$. Chemical profiles in d-f and j-l were derived from EDS scan areas in the range of 30000 nm^2 for out-of-plane and 3000 nm^2 for in-plane quantification.

comparison to STEM images with the crystalline / amorphous interface horizontal. Visualisation of one single in-depth grain is achieved by the 10 nm thick reconstruction of atomic positions. The mass-spectra for each atom probe measurement can be found in the Supplementary Material. Fig. 6a and Fig. 7a show FCC Al layers with Ni-rich nanoclusters as well as H- and O-enriched AlO_xH_y interlayers in the case of $\text{Al}_{98}\text{Ni}_2 / \text{AlO}_x\text{H}_y$ as well as $\text{Al}_{95}\text{Ni}_5 / \text{AlO}_x\text{H}_y$, respectively. In fact, the composition of the crystalline FCC Al-Ni layers of $\text{Al}_{98}\text{Ni}_2$ can be quantified as $\text{Al}_{92.7 \pm 1.9}\text{Ni}_{3.3 \pm 1}$ with $0.6 \pm 0.3 \text{ at.}\%$ O, $2.5 \pm 1.2 \text{ at.}\%$ H, $0.4 \pm 0.2 \text{ at.}\%$ C, and $0.5 \pm 0.3 \text{ at.}\%$ N, as shown in the composition profile in Fig. 6b. In the case of $\text{Al}_{95}\text{Ni}_5 / \text{AlO}_x\text{H}_y$, Fig. 7b reveals the composition of FCC Al-Ni layers to be $\text{Al}_{87 \pm 2.6}\text{Ni}_{6.7 \pm 1.5}$ with 1.2 ± 0.6 ,

$4.2 \pm 1.1 \text{ at.}\%$, $0.4 \pm 0.3 \text{ at.}\%$, and $0.5 \pm 0.3 \text{ at.}\%$ O, H, C, and N, respectively. The Ni-rich nanoclusters are displayed by 6 and 10 at.% Ni isoconcentration surfaces (i.e. within double to triple the average Ni concentrations) in the case of $\text{Al}_{98}\text{Ni}_2$ and $\text{Al}_{95}\text{Ni}_5$ layers, respectively. In neither case does APT reveal higher Ni concentrations of vertical Al-Al grain boundaries or the crystalline / amorphous interface, which was previously assumed based on the results from STEM-EDS in Fig. 4 and Fig. 5.

The amorphous AlO_xH_y layers show an enrichment in O and H and seem to be quasi-continuous as depicted in Fig. 6a and Fig. 7a, respectively. Coupled with nominal $\text{Al}_{98}\text{Ni}_2$ layers, their composition can be quantified as approximately $\text{Al}_{74.1}\text{H}_{11.4}\text{O}_{6.9}\text{Ni}_{4.9}\text{C}_{1.3}\text{N}_{1.4}$, visualised via a



(caption on next column)

Fig. 5. High Magnification STEM-EDS mapping of the $\text{Al}_{95}\text{Ni}_5$ / AlO_xH_y thin film: (a) HAADF-EDS, (b) Ni atomic fraction, as well as (c) in-plane HAADF vs. Ni atomic fraction profile over a few grains, and (d) out-of-plane HAADF vs. Ni atomic fraction profile over 2 bilayer periods.

composition profile in Fig. 6c. In the case of $\text{Al}_{95}\text{Ni}_5$, the chemistry of amorphous AlO_xH_y can be quantified as $\text{Al}_{73.7}\text{H}_{10.4}\text{Ni}_{8.4}\text{O}_{5.8}\text{C}_{0.7}\text{N}_{1.0}$, as illustrated in Fig. 7c. The out-of-plane composition profiles in Fig. 6c and Fig. 7c reveal similar Ni contents of up to ~ 8 at.% in AlO_xH_y for both $\text{Al}_{98}\text{Ni}_2$, but not for $\text{Al}_{95}\text{Ni}_5$. Yet, the Ni content increases from ~ 5 at.% in the Al-Ni grains to ~ 8 at.% in AlO_xH_y for $\text{Al}_{98}\text{Ni}_2$, while the Ni content is similarly ~ 8 at.% in the Al-Ni grains as well as in AlO_xH_y for $\text{Al}_{95}\text{Ni}_5$. Consequently, saturation of the AlO_xH_y interlayers occurs at Ni content of ~ 8 at.%. Nitrogen in both cases might stem from the purifier to purge the ALD pump and eventual backstreaming. Further, there are also C and other impurities detected from both samples. Mean chemical compositions of the amorphous interlayers here are derived from the composition profiles visible in Fig. 6 and Fig. 7 and standard deviations are in the range of those quantified for the crystalline layers.

This is the first study that utilises APT to 3D track hydrogen and oxygen in thin 1 nm AlO_xH_y interlayers. However, the H content can be understood as an upper boundary value due to the likely contribution of residual gas from the analysis chamber. Recently, elastic recoil detection analysis / Rutherford backscattering spectrometry (ERDA / RBS) has been employed for AlO_xH_y , grown by ALD [39,40,53] and Byloff et al. [53] obtained $\text{Al}_{0.24}\text{O}_{0.48}\text{H}_{0.28}$ for 75 nm-thick films grown under identical conditions as in the present work, but on polyimide. In other room temperature ALD studies, a hydrogen content of ~ 22 at.% was found for 130 nm AlO_xH_y on Si substrates, when utilising TMA and heavy water [40] as well as a H / Al ratio of 1.0 – 2.0 for 40 nm, when deposited by TMA and $\text{DI-H}_2\text{O}$ on Si substrates [39]. These three studies propose close-to-equiatomic Al and H content in the range of 24 ± 4 at.% with remaining oxygen of 52 ± 8 at.%. Thus, underestimation of both hydrogen and oxygen is expected for the here measured compositions of $\text{Al}_{74.1}\text{H}_{11.4}\text{O}_{6.9}\text{Ni}_{4.9}\text{C}_{1.3}\text{N}_{1.4}$ and $\text{Al}_{73.7}\text{H}_{10.4}\text{Ni}_{8.4}\text{O}_{5.8}\text{C}_{0.7}\text{N}_{1.0}$ within the thin 1 nm interlayer, which is likely also affected by Ni diffusion. Additionally, chemical intermixing artefacts and reduced quantifiability are expected from 1 nm interlayers due to the common phenomenon of trajectory aberrations [54]. Therefore, APT data of oxygen and hydrogen has to be interpreted qualitatively. Additionally, the 10 nm analysis cylinder for APT quantification agrees with STEM imaging in the visibility of thin interlayers as “twisted” layers due to layer overlapping within the depth of the cylinder. For better visualisation of the interlayer shape in APT images the reader is referred to the online version of the article. Yet, there is a certain interlayer diffuseness visible that was not observed in STEM. Nevertheless, APT-driven 3D detection of hydrogen in these amorphous AlO_xH_y films provides an emerging experimental benchmark that can be directly correlated with atomistic simulations [55], enabling a mechanistic understanding of hydrogen’s role in modifying local bonding, network connectivity, and material properties.

While there are plenty of studies utilising STEM to analyse interface-engineered nanocrystalline Al alloys (e.g., [6,11,13]), APT is not an often-exploited technique in this field. Zhou et al. [56] performed APT on Ni_{99}P_1 and Ni_{96}P_4 alloys to visualise P agglomeration at grain boundaries. The observation from APT allowed them to derive thermodynamic stabilisation of Ni-Ni grain boundaries with < 0.2 at.% P agglomeration. Ga^+ -FIB preparation of Al APT specimens is known to severely impede the analysis of interfaces – significantly increasing the uncertainty of preparation induced microstructure changes [57]. APT unravelled Ga decoration of Guinier-Preston zones at the matrix-precipitate-interface in an Al-Mg-Zn-Cu alloy [57,58], as well as Ga chemically marking amorphous Al-Mn phases in an Al-Mn alloy [59], and Ga decorating dislocation regions in Al-Mg [60]. Elsewhere, Zhao et al. [58] were able to perform APT on an Al-Mg-Zn-Cu alloy, where

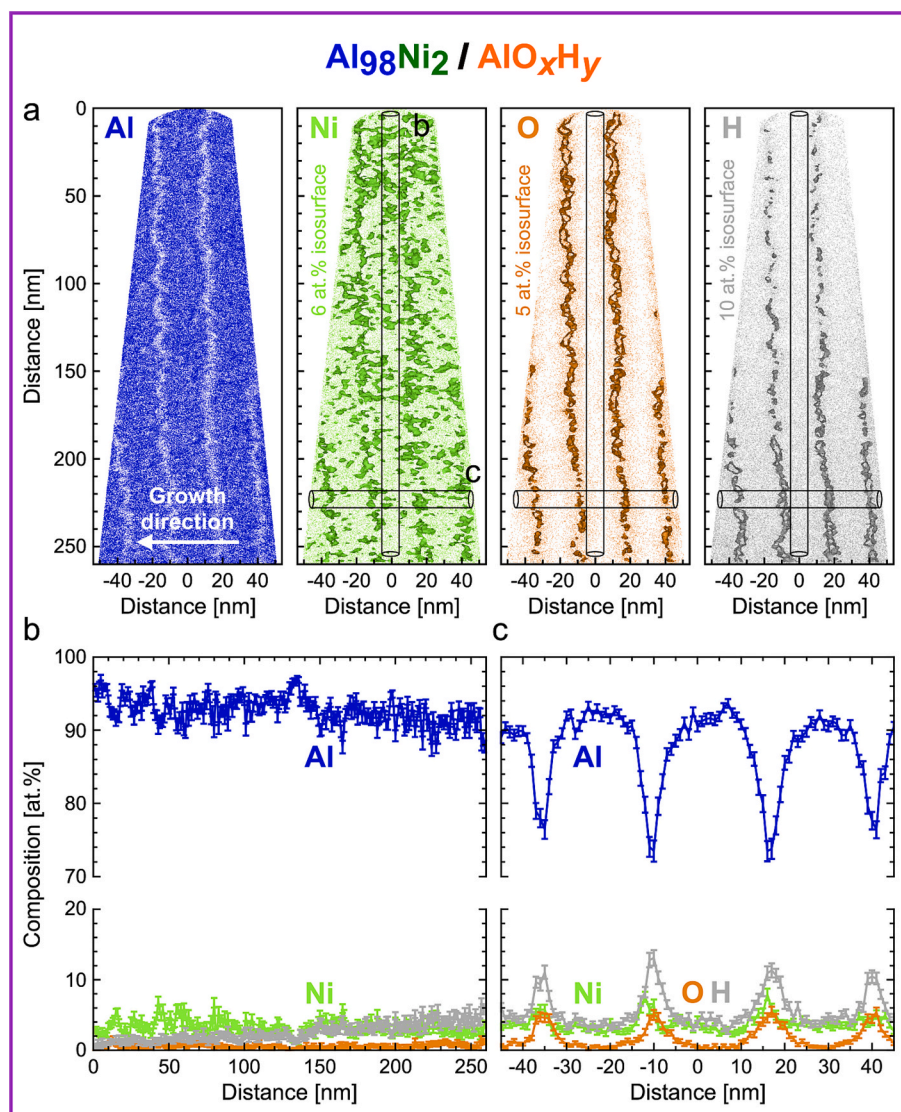


Fig. 6. APT reconstruction of atomic positions (10 nm slice) from the $\text{Al}_{98}\text{Ni}_2 / \text{AlO}_x\text{H}_y$ thin film including (a) Al, O, Ni, and H as well as (b) in-plane and (c) out-of-plane composition profiles from the cylinders with a diameter of 10 nm, indicated in (a).

6 to 10 at.% isoconcentration surfaces of Zn validated grain boundary decoration; notably, the Al-Al grain boundaries were found to be enriched in Cu, Zn, and Mg in the as-quenched state. Recently, Yang *et al.* [61] applied APT to reveal the partitioning of solute elements as well as formation of NiAl nanoparticles with less than 3 nm size and 2.4% volume fraction in high strength ductile steel. Previously, De Geuser and Gault [62] demonstrated that the effective accurate spatial resolution of APT in comparison to small-angle X-ray scattering (SAXS) is highly specific to the material system and limited to 1 nm.

Here, APT shows nanocluster formation of Ni-rich phases in the FCC Al matrix – not visible through STEM – with local enrichment in Ni up to 13 and 19 at.% in $\text{Al}_{98}\text{Ni}_2 / \text{AlO}_x\text{H}_y$ and $\text{Al}_{95}\text{Ni}_5 / \text{AlO}_x\text{H}_y$, respectively, Fig. 8a&b. While the Al-Ni phase diagram would predict phase separation between FCC Al and orthorhombic Al_3Ni with 2 and 5 at.% Ni, the latter phase was previously not reported to form below 380 °C [33]. Additionally, APT complements the dataset from STEM-EDS with qualitative hydrogen estimation as upper boundary values. This is a major advantage in the analysis of interface-engineered materials, and an aspect which was not considered in recent decades, where the discussion above emphasised the focus often laid on STEM-EDS for chemical mapping. Yet, state-of-the-art research requires the need of hydrogen analysis in novel structural materials towards e.g., hydrogen-tolerant

alloy design [63]. Here, we are expecting the AlO_xH_y to be a weaker diffusion barrier than dense Al_2O_3 [39] and thus, allow Ni diffusion into the AlO_xH_y , which was visible both through STEM-EDS as well as APT characterisation. To facilitate further reading, the STEM-EDS- and APT-derived chemistries of both crystalline and amorphous layers of this work are not repeated in the following, unless necessary for the discussion – rather, the nominal compositions are used.

3.4. Mechanical properties: Nanoindentation

Nanoindentation was performed to evaluate the influence of Ni addition on the hardness of $\text{Al}_{100-z}\text{Ni}_z / \text{AlO}_x\text{H}_y$ thin films. Table 1 shows increasing film hardness with alloying of up to 5 at.% Ni to the crystalline FCC Al matrix – ultimately reaching almost 5.3 GPa of nanoindentation hardness. In fact, the Al grains in undoped Al / AlO_xH_y show a nanoindentation hardness of 2.7 ± 0.1 GPa, whilst already 2 at.% Ni induces a film hardening up to 4.9 ± 0.2 GPa – hence an 82% and 98% increase in hardness for 2 and 5 at.% Ni, respectively, compared to the unalloyed state. It is emphasised that the current investigation focuses on hardness measurements as a relatively fast and well-established screening option for mechanical strength of nanocrystalline materials. Future work will shed more light on the whole mechanics portfolio

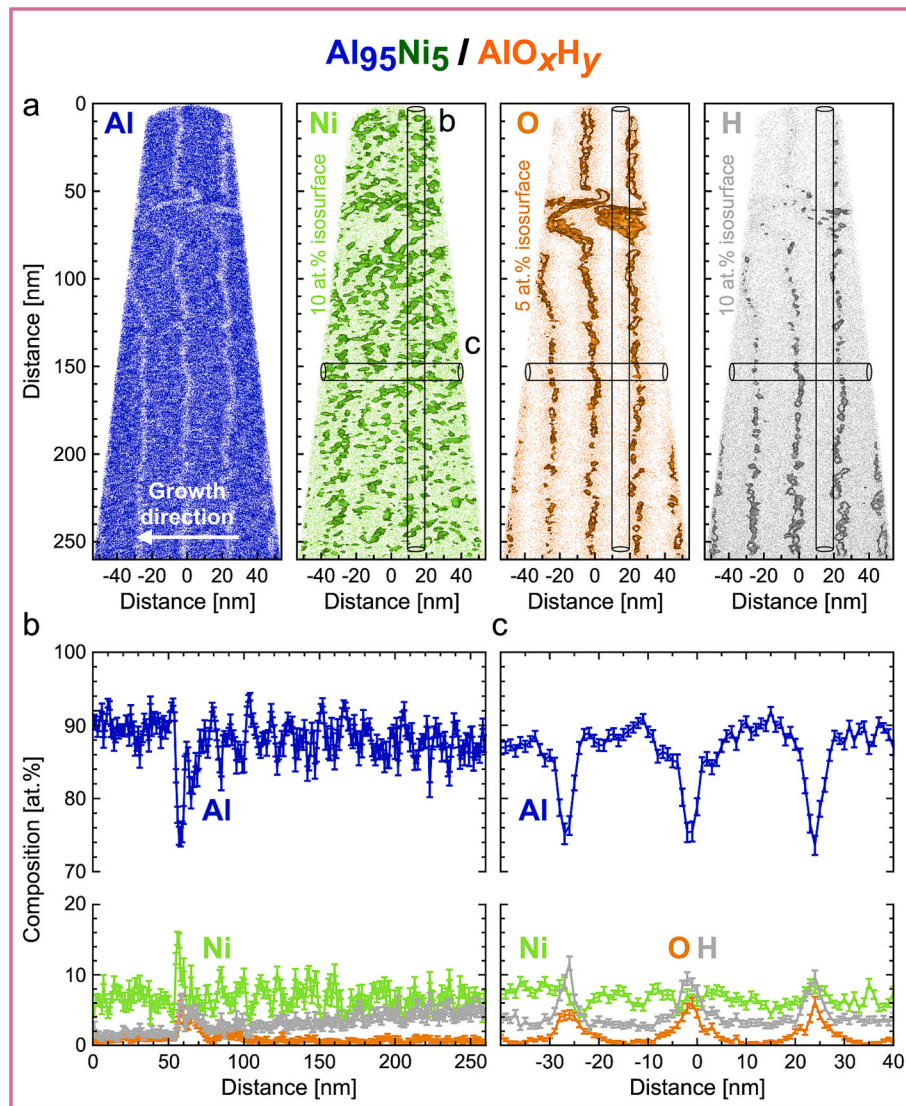


Fig. 7. APT reconstruction of atomic positions (10 nm slice) from the $\text{Al}_{95}\text{Ni}_5 / \text{AlO}_x\text{H}_y$ thin film including (a) Al, O, Ni, and H as well as (b) in-laminate-plane and (c) out-of-plane composition profiles from the cylinders with a diameter of 10 nm, indicated in (a).

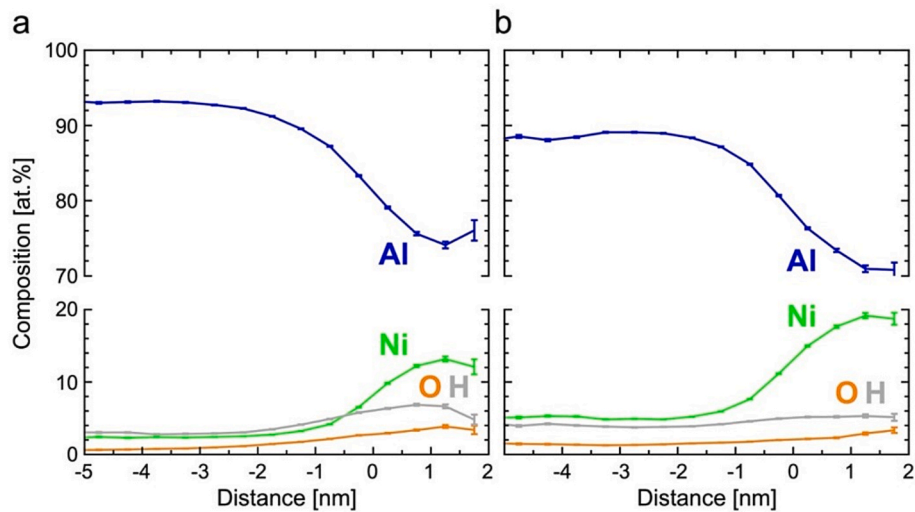


Fig. 8. Proximity histograms of Ni-rich regions in (a) $\text{Al}_{98}\text{Ni}_2 / \text{AlO}_x\text{H}_y$ and (b) $\text{Al}_{95}\text{Ni}_5 / \text{AlO}_x\text{H}_y$ thin films.

Table 1

Evaluation of mechanical properties of $\text{Al}_{100-z}\text{Ni}_z / \text{AlO}_x\text{H}_y$. Nanoindentation hardness of each sample as well as calculated strength contributions from the relevant microstructure and chemistry variations.

Sample	Measured hardness (GPa)	Calculated strength contribution				
		σ_{CLS} (GPa)	σ_{Tay} (GPa)	σ_{SSS} (GPa)	σ_{Bow} (GPa)	σ_{Cut} (GPa)
Al / AlO_xH_y	2.7 ± 0.1	0.8	0.1			
$\text{Al}_{98}\text{Ni}_2 / \text{AlO}_x\text{H}_y$	4.9 ± 0.2	1.3	0.4	<0.01	0.2–2.2	0.2–1.6
$\text{Al}_{95}\text{Ni}_5 / \text{AlO}_x\text{H}_y$	5.3 ± 0.1	1.8	0.9	<0.01	0.2–4.7	0.2–2.4

including the role of deformation mechanism energy and activation volume, plasticity (of thin 1 nm AlO_xH_y), and fracture toughness, which are beyond the scope of discussion here. In the work of Baral *et al.* [23], the authors applied finite element simulations to capture the mechanical response of Al / Al_2O_3 nanolaminated thin films. The authors report on strengthening from confined plastic deformation in Al layers through stiff Al_2O_3 layers, where simulations show the highest shear stress near Al / Al_2O_3 interfaces. Similarly, one might ask where strength in these nanolaminated $\text{Al}_{100-z}\text{Ni}_z / \text{AlO}_x\text{H}_y$ thin films originates from there. To what extent can the individual contributions of crystalline / amorphous interfaces, grain size, and nanocluster formation to mechanical strengthening be independently resolved? To this purpose, strength contributions were calculated from the following strengthening mechanisms commonly applied to nanolaminated and nanocrystalline metals: FCC Al grain size effects in the nanolaminated architecture σ_{CLS} (confined layer slip), dislocation network density σ_{Tay} (Taylor hardening), solute-matrix interaction σ_{SSS} (solid solution strengthening), as well as secondary phases in the matrix requiring Orowan bowing σ_{Bow} and/or particle cutting σ_{Cut} by matrix dislocations, respectively.

STEM imaging did not reveal growth twin formation in the Ni-containing materials. Thus, we do not expect twin boundaries as dislocation obstacles in $\text{Al}_{100-z}\text{Ni}_z / \text{AlO}_x\text{H}_y$. Yet, notably, nanotwinned (nt)-AlNi thin films with > 5 GPa hardness and as-deposited growth twins were recently reported to arise due to a stacking fault energy reduction from 120 mJ m^{-2} of pure Al down to 112 mJ m^{-2} in the case of $\text{Al}_{98}\text{Ni}_2$ [45]. Furthermore, nanocrystalline Al with grain size below 25 nm was reported to soften due to a shift in deformation mechanism from dislocation-mediated plasticity to grain boundary sliding – yielding the so-called inverse Hall-Petch effect [64]. Yet, lateral grain refinement to $13 \pm 4 \text{ nm}$ and $8.7 \pm 2.6 \text{ nm}$ lateral FCC Al grain size upon Ni-addition of 2 and 5 at.% here reveals continued strengthening, contrary to any grain boundary-mediated deformation mechanisms.

The remaining short list of traditional strengthening mechanisms relevant for this architecture of nanolaminated material can therefore be specifically expressed by the following equations [15,16,20,65–69]:

$$\sigma_{\text{CLS}} = M \frac{Gb}{8\pi h} \left(\frac{4-\nu}{1-\nu} \right) \ln \frac{ah'}{b} - \frac{\gamma}{h} + \frac{Gb}{L(1-\nu)} \quad (1)$$

$$\sigma_{\text{Tay}} = M\alpha Gb\sqrt{\rho} \quad (2)$$

$$\sigma_{\text{SSS}} = M\phi G\epsilon^{3/2} c^{2/3} \quad (3)$$

$$\sigma_{\text{Bow}} = 0.4M \frac{Gb}{\pi\chi} \ln \left(\frac{2r_s}{b} \right) (1-\nu)^{-0.5} \quad (4)$$

$$\sigma_{\text{Cut}} = \sqrt{\frac{GbG_{\text{particle}}}{2C\chi}} \quad (5)$$

For architectural size effects in nanolaminated materials, especially with opposing extremes of crystallinity (crystalline / amorphous), confined layer slip (CLS) strengthening was often found as the root cause [15–17,20]: strength results from enhanced dislocation bowing through

nanolaminating nanocrystalline metal layers of less than 50 nm thickness alternated with amorphous interlayers. Experimental comparison of crystalline / crystalline Cu / Zr and crystalline / amorphous Cu / CuZr nanolaminates have demonstrated the validity of the CLS model for thin amorphous interlayers [70]. Experiment and simulation have approached the mechanism through thin strain-accommodating amorphous layers and dislocation nucleation from adjacent interfaces [70–72]. Although sub-10 nm amorphous layers are generally thought incapable of sustaining localized shear [73,74], thin ALD oxides might give rise to stress concentrations at the crystalline / amorphous interfaces [75] and shear transformation zones [76].

The conventional CLS model proposes a critical layer thickness governing maximum strength [15]. However, Huang, Beyerlein, and Zhou [77] applied atomic-scale simulations on nanolayered Cu / Nb bilayer systems investigating the influence of layer thickness and lateral grain size variation on the dominant dislocation-governed deformation mechanism. The authors' calculations predicted first yielding to be controlled by the FCC Cu grain size rather than the layer thickness: flow stress at constant layer thickness decreases almost linearly with decreasing grain size when layer thicknesses and grain sizes of 1–15 nm and 2.5–40 nm were respected. This observation is in agreement with the commonly observed inverse Hall-Petch effect for nanocrystalline metals [64] towards grain boundary-mediated deformation.

Here, an apparent change of FCC Al layer thickness to lateral grain size is observed that cannot be overlooked: from equiaxed state (Al / AlO_xH_y) to significantly reduced lateral grain size when Ni-doped. $\text{Al}_{98}\text{Ni}_2 / \text{AlO}_x\text{H}_y$, and $\text{Al}_{95}\text{Ni}_5 / \text{AlO}_x\text{H}_y$ show enhanced nanoindentation hardness despite lateral grain size refinement in the range of expected weakening [64]. Therefore, the CLS model limitations on the role of layer thickness vs. lateral grain size need to be considered carefully in the following analysis. The CLS model in Eq. (1) applies Taylor factor M (3 for randomly oriented FCC metals), shear modulus G , Burgers vector b (0.2864 nm), effective layer thickness parallel to [110] slip direction h' ($\sqrt{3} \times$ lateral grain size [22]), Poisson ratio ν (0.3 for FCC Al), geometrical factor α (~ 0.6 [20]), crystalline / amorphous interface stress γ , FCC Al(–Ni) layer thickness h (25 nm), and dislocation source length L (here approximated by layer thickness). The shear moduli for 2 and 5 at.% Ni containing FCC Al–Ni are approximated by linear interpolation between FCC Al and Orthorhombic Al_3Ni with $G_{\text{Al}} = 26 \text{ GPa}$ and $G_{\text{Al}_3\text{Ni}} = 59 \text{ GPa}$ [78], respectively. The interface stress for crystalline / amorphous interfaces in CLS was previously assumed around $0.5 - 1.1 \text{ J m}^{-2}$ with e.g., Cu / CuZr nanolaminates around 0.6 J m^{-2} [20,79]. Here, the $\text{Al}_{100-z}\text{Ni}_z / \text{AlO}_x\text{H}_y$ interface stress of the natural Al / AlO interface is assumed higher and approximated by the works of separation of an Al-rich Al / $\alpha\text{-Al}_2\text{O}_3$ interface with 1.43 J m^{-2} [80]. Inserting the values of G , h' , and L for $\text{Al}_{100-z}\text{Ni}_z$, CLS predicts around 0.8 GPa, 1.3 GPa, and 1.8 GPa strengthening for nanolaminated Al / AlO_xH_y , $\text{Al}_{98}\text{Ni}_2 / \text{AlO}_x\text{H}_y$, and $\text{Al}_{95}\text{Ni}_5 / \text{AlO}_x\text{H}_y$, respectively. As for this specific strength / hardness contribution calculation, the list of parameters for each mechanism can be found in the Supplementary Material.

Regarding the nature of AlO_xH_y versus work on Al_2O_3 [22,23], the presence of H is expected to weaken the interlayers due to a reduced bonding energy of the Al–H bonds compared to strong ionic-covalent Al–O bonds in pure Al_2O_3 . Schneider *et al.* [81] reported H-induced crystallisation and 53% softening of reactive sputter deposited AlO_xH_y thin films with up to 13.9 at.% H. Yet here we are considering ultra-thin amorphous AlO_xH_y by ALD embedded between nanocrystalline Al layers, where a future study will focus on the deformation mechanisms more closely and the role of individual microstructure features, especially the role of AlO_xH_y and Al_2O_3 as potentially impenetrable barriers to dislocation motion [82]. It is noted that in nanolaminates incorporating thin amorphous interlayers, the assumption of rigid interfaces inherent to confined layer slip models can be altered, as these interlayers may act as plastically active, compliant regions capable of accommodating dislocation activity via shear transformation processes depending

on the interface structure [83,84]. A manuscript is currently in preparation that discusses the role of amorphous AlO_xH_y as rigid barriers. Concerning the role of Ni in the AlO_xH_y interlayers, Ni-reinforced Al_2O_3 composites were recently reported to possess enhanced strength and toughness due to ductile Ni particles absorbing deformation energy, whereas Ni was also found to increase porosity [85]. Here, a similar effect of Ni can be expected as APT in Fig. 6 and Fig. 7 show similar formation of Ni-rich nanoclusters in the vicinity of the amorphous AlO_xH_y interlayers.

Taylor hardening occurs due to increased dislocation density [65], modelled by Eq. (2) with constant α (~ 0.24 [22]) and the dislocation density ρ . The dislocation densities here are calculated by applying the Williamson Smallman method [86] to (111) FCC Al diffraction visualised in Fig. 3a X-ray diffractograms following the relationship:

$$\rho = \frac{n}{D^2} \quad (6)$$

with n dislocations per grain (1 here for minimum dislocation density) and D grain size applying the Scherrer equation to the (111) FCC Al FWHM from Fig. 3a. Assuming one dislocation per grain here, the dislocation densities derived should be seen as a lower bound. The Scherrer equation reveals roughly 41, 15, and 8 nm of grain size for Al / AlO_xH_y , $\text{Al}_{98}\text{Ni}_2$ / AlO_xH_y , and $\text{Al}_{95}\text{Ni}_5$ / AlO_xH_y , respectively. Likewise, dislocation densities around $6 \times 10^{14} \text{ m}^{-2}$, $5 \times 10^{15} \text{ m}^{-2}$, and $2 \times 10^{16} \text{ m}^{-2}$ can be obtained for Al / AlO_xH_y , $\text{Al}_{98}\text{Ni}_2$ / AlO_xH_y , and $\text{Al}_{95}\text{Ni}_5$ / AlO_xH_y , respectively. Thus, the increased dislocation density from adding up to 5 at.% Ni to the crystalline FCC Al layers may result in film strengthening of 0.1–0.9 GPa.

Regarding solution strengthening, Labusch [68,69] proposed a model applicable for nanocrystalline metals enriched with nanoclusters as shown in Eq. (3): φ is a constant (1/550 for FCC metals), ϵ the interaction factor (change in shear modulus and lattice parameter upon alloying), and c the Ni concentration (0.02 and 0.05). Inserting the given numerical values into Eq. (3), solid solution strengthening by 2 and 5 at.% Ni in FCC Al towards FCC Al-Ni solid solution might not exceed 0.01 GPa. Hence, the strengthening from solid solution Al-Ni is negligible here compared to overall film hardness (in excess of 5 GPa). For dislocations encountering matrix particles, Orowan [66] bowing is a relevant mechanism. It is emphasised that Ni-rich nanoclusters are formed in the FCC Al matrix based on APT data and thus, the mechanisms dislocation – particle focusses on matrix obstacles rather than grain boundary pinning. For this calculation we assume the Ni-rich nanoclusters as “strong” non-shearable impenetrable particles that require glide dislocation bending to an angle $< 100^\circ$, thus strength can be derived following Eq. (4) as proposed in [87]. In addition to already above-mentioned variables, the model in Eq. (4) applies intersection radius of particles r_s , and inter-particle spacing χ derived from volume fraction f as in [87]:

$$\chi = r_s \left(\sqrt{\pi/f} - 2 \right) \quad (7)$$

However, particle radii and volume fractions can only be approximated from APT data, where both values are sensitive to applied iso-concentration surfaces as visualised in Fig. 6 and Fig. 7. Yet, the histograms in Fig. 8 show Ni-enrichment reaching more than 1 nm in lateral dimension, thus a range of r between 1 and 5 nm is assumed. An upper bound volume fraction for the Ni-rich nanoclusters respecting the almost Ni-free Al matrix would be around 11 and 25%, for globally 2 and 5 at.% Ni dissolved in Al, respectively. Following these considerations, σ_{Bow} for $\text{Al}_{98}\text{Ni}_2$ / AlO_xH_y may lie in the range of 0.2 GPa ($r_s = 4.1 \text{ nm}$, $f = 1\%$) to 2.2 GPa ($r_s = 0.8 \text{ nm}$, $f = 11\%$), while for $\text{Al}_{95}\text{Ni}_5$ / AlO_xH_y in the range of 0.2 GPa ($r_s = 4.1 \text{ nm}$, $f = 1\%$) to 4.7 GPa ($r_s = 0.8 \text{ nm}$, $f = 25\%$).

Cutting particles is the competing mechanism to Orowan bowing: Ansell and Lenel [67] proposed a model for dislocations cutting particles dispersed in the matrix. G_{particle} , and C in this Eq. (5) refer to shear modulus of particles, and the constant of proportionally dependent on

the lattice perfection degree of dispersed particles. Here, G_{particle} cannot be determined exactly, as no other phase than FCC Al was detected by XRD, SAED, and HR-STEM, therefore G_{particle} being approximated by an upper and lower bound. Both STEM-EDS and APT showed oxygen contents below 5 at.% and thus low probability for ternary oxide or hydroxide formation. Shi *et al.* [78] performed DFT calculations on various intermetallic Al-Ni compounds. For low Ni contents, Al_3Ni showed the lowest shear modulus around 59 GPa. Thus, a lower and upper bound for G_{particle} might lie in the range of $G_{\text{Al}} = 26 \text{ GPa}$ and $G_{\text{Al}_3\text{Ni}} = 59 \text{ GPa}$, respectively. The inter-particle spacing χ ranges are the same as for Orowan evaluation above. Thus, lower and upper bound strengthening for $\text{Al}_{98}\text{Ni}_2$ / AlO_xH_y by the cutting mechanism can be derived around 0.3 – 1.6 GPa ($G_{\text{Al}_3\text{Ni}}$, $r_s = 0.8 - 4.1 - 5 \text{ nm}$, $f = 1 - 11\%$) and 0.2 – 1.1 GPa (G_{Al} , $r_s = 0.8 - 4.1 \text{ nm}$, $f = 1 - 11\%$). For $\text{Al}_{95}\text{Ni}_5$ / AlO_xH_y , dislocations cutting particles can induce strength around 0.3 – 2.4 GPa ($G_{\text{Al}_3\text{Ni}}$, $r_s = 0.8 - 4.1 \text{ nm}$, $f = 1 - 25\%$) and 0.2 – 1.6 GPa (G_{Al} , $r_s = 0.8 - 4.1 \text{ nm}$, $f = 1 - 25\%$).

Although it would appear that Al-Ni nanoclusters lie in the range of the cutting mechanism [88] being dominant, over Orowan bowing, the lowest resolved stress differs with phase and geometric parameters.

Substantial strengthening can be derived from the textbook models on dislocation – nanocluster interaction. Yet, these models need to be put into perspective with current (simulation-based) advances in dislocation – obstacle interactions: do they agree? Van Swygenhoven *et al.* [89] applied MD simulations to postulate pronounced impediment of propagating dislocations due to misfit strain in the vicinity of nanoclusters in FCC metals. The modeling feasibility of nanoclusters was confirmed by atomistic simulations predicting flow stress in Al-Cu alloys [88,90]. In fact, simulated Guinier-Preston zones in an Al-4 wt% Cu alloy were found to be in good agreement with experimental data: at 300 K both experiment and atomistic simulation predicted roughly 50 MPa flow stress [90]. In precipitation-strengthened AlMgSi, Hu and Curtin [91] simulated a critical resolved shear stress of Orowan bowing around Mg_2Si precipitates with $f \leq 1.10\%$ up to 165 MPa. Here however,

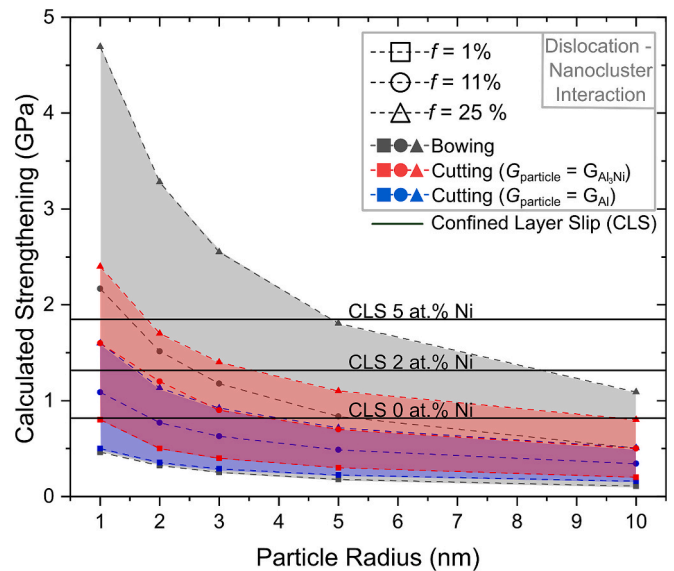


Fig. 9. Calculated strength contribution from dislocation – particle interaction when Ni-rich nanoclusters are seen as particles. The particle radii and volume fractions are approximated from APT data in Fig. 6, Fig. 7, and Fig. 8, while bowing and cutting contributions are calculated from Eq. (4) and (5). Bowing strengthening is visualized by the gray area. The two cutting contributions can be seen as a lower bound when $G_{\text{particle}} = G_{\text{Al}}$ (blue area) and upper bound when $G_{\text{particle}} = G_{\text{Al}_3\text{Ni}}$ (red area). The horizontal black lines refer to CLS strengthening from Eq. (1) for the three different architectures. (For interpretation of the references to colour in this figure legend, the reader is referred to the web version of this article.)

at $f = 1\%$ Ni-rich nanoclusters, several hundred megapascal strengthening was calculated from dislocation – nanocluster interaction by Orowan bowing. To facilitate the comparison, Fig. 9 shows calculated strength contributions comparing the dislocation bowing and cutting mechanisms as a function of particle radius as well as the three strengthening values derived from CLS. Particle radii from 1 to 10 nm were considered. It is emphasized that the $\sqrt{1/\chi}$ dependency in Eq. (5) results in similar stress profiles of the bowing and cutting mechanisms. Here, two major trends in particle-dislocation interaction are visualised: for a volume fraction of 1%, both cutting and bowing show similar stress levels; and for higher volume fractions of 11% and 25%, the cutting mechanism is preferential. As the mechanism with the lowest critical resolved stress becomes active first, several hundred megapascal up to approximately 1 GPa strengthening is expected. Yet, MD simulations were able to confirm several hundred megapascals strengthening from nanoclusters in a Cu-Ta alloy [92–94]. In fact, coherent Ta nanoclusters were found to pose obstacles to grain boundary sliding and rotation, as well as to dislocation nucleation – ultimately being responsible for 65% of the alloy's 1.3 GPa true strength.

Table 1 shows that strengthening in the nanolaminated $\text{Al}_{100-z}\text{Ni}_z / \text{AlO}_x\text{H}_y$ thin films may stem primarily from a combination of CLS and particle cutting. Ni-addition affects both confinement of effective crystallite size parallel to the [110] slip direction in CLS and the formation of Al-Ni nanoclusters. The strength contribution of the particles is predicted to exceed that of CLS only for particle radii below approximately 3 nm. Ultimately, the more than 5.2 GPa of nanoindentation hardness in the case of $\text{Al}_{95}\text{Ni}_5 / \text{AlO}_x\text{H}_y$ is a consequence of interacting dislocation strengthening mechanisms that cannot be easily decoupled.

3.5. Microstructure design route evaluation

Fig. 10 shows a nanoindentation hardness comparison of high-performance nanocrystalline Al alloys as a function of the smallest inverse square-root grain size (Hall-Petch plot). It is emphasised that the application of a Taylor factor of 3 to compare yield strength and nanoindentation hardness represents a conventional approximation for randomly oriented FCC materials, despite the possibility of deviations in nanocrystalline and nanolaminated systems arising from altered grain boundary and interface-dominated deformation mechanisms [95,96]. Furthermore, pile-up is observed here at the indent perimeter, increasing the effective contact area beyond that assumed in the analysis, hence resulting in a slight overestimation of hardness, which may hamper direct comparison with literature data. It is evident that the strongest thin film of this work, $\text{Al}_{95}\text{Ni}_5 / \text{AlO}_x\text{H}_y$ with bilayer period of

25 / 1 nm, is certainly one of the strongest interface-engineered nanocrystalline Al materials reported so far. Among nanolaminates, Baral et al. [23] showed nanoindentation hardness of crystalline – amorphous Al / Al_2O_3 with the lowest comparable volume fraction Al_2O_3 (44 / 5 nm, $f_{\text{Al}_2\text{O}_3} = 10.2\%$) of approximately 2.6 GPa, which is comparable to the pure Al / AlO_xH_y here. Yet, Ni addition and Ni-rich nanocluster formation here add significant strengthening, comparable to previously reported strengthening by Al_9Co_2 precipitates in additively manufactured Al-Co [5]. Comparing indentation values here to interface-engineered Al alloys with altered chemistry of grain boundaries [6,11,13,97], the $\text{Al}_{95}\text{Ni}_5 / \text{AlO}_x\text{H}_y$ shows < 10-nm (lateral) grain sizes and competes with previously reported 5.2 GPa for an interface-engineered Al-Ni-Ce tested at room temperature. We consider that that high nanoindentation hardness is a consequence of both crystalline / amorphous interfaces [15] as well as precipitation strengthening by nanoclusters in the metallic layers. Yet, such complexity requires further investigation of the strengthening mechanisms, including determination of the activation volume and energy of the rate controlling deformation mechanism.

Ultimately, Fig. 10 emphasises that previous studies on various nanocrystalline Al designs already showed excellent nanoindentation hardness. Notably, nanotwinned (nt) Al-Ni alloys with sub-10-nm grain size as well as interface-engineered nanocrystalline Al-Ni-Ce and Al-Fe alloys were able to achieve > 5 GPa nanoindentation hardness [6,34,45]. The latter Al-Ni-Ce and Al-Fe alloys reported to be even thermally stable up to more than 200 °C by the amorphous grain boundary phases acting as stabilisers. However, the incorporation of ultrathin AlO_xH_y interlayers via ALD offers a promising route to further enhance the thermal stability of nanocrystalline Al beyond this, whilst achieving good mechanical properties. Naturally-occurring amorphous metallic grain boundary phases are not as thickness- and chemistry-controllable as the artificial homogenous ALD layers here. By precisely controlling the interface structure at the atomic scale, this PVD / ALD design strategy holds potential to suppress out-of-plane grain boundary mobility more effectively than conventional bulk-stabilised systems — an aspect that will be critical for extending mechanical performance of nanocrystalline Al to elevated temperatures. Here, the dual-route-tailoring dictates exactly the out-of-plane dimension, with an additional degree of microstructural control in-plane, hopefully enabling simultaneous optimisation of mechanical performance and thermal stability.

4. Conclusions

In conclusion, we have presented an approach to combine PVD of Al with low amounts of Ni, and ALD of AlO_xH_y , towards designing a dual-route-tailored nanolaminated $\text{Al}_{100-z}\text{Ni}_z / \text{AlO}_x\text{H}_y$ thin film with ultra-fine feature sizes. The findings from macroscopic XRD, high-resolution microscopy through TEM and APT, as well as quasi-static nano-indentation allow us to conclude the following points:

- The addition of low amounts of Ni to the crystalline Al layer, up to $\text{Al}_{95}\text{Ni}_5 / \text{AlO}_x\text{H}_y$, with comparable 25 / 1 nm bilayer period, does not induce phase formation other than FCC Al while retaining ultra-fine lateral grain sizes as low as 9 nm and smoother crystalline / amorphous interfaces.
- Rather than enriching the Al-Al grain boundaries with Ni segregations in a *complexion-engineering* approach, we identified the formation of Ni-rich nanoclusters in the crystalline matrix and Ni-enrichments in the amorphous AlO_xH_y layer.
- To that extent, APT was used to track the formation of Al-Ni nanoclusters with up to 20 at.% local Ni-enrichment, and size in the range of a few nanometres, to enrich the dataset of STEM-EDS, which predicted Al-Al grain boundary decoration by Ni.
- Nanoindentation measurements revealed up to 5.3 GPa hardness for $\text{Al}_{95}\text{Ni}_5 / \text{AlO}_x\text{H}_y$. As a counterpart to the experimental observations,

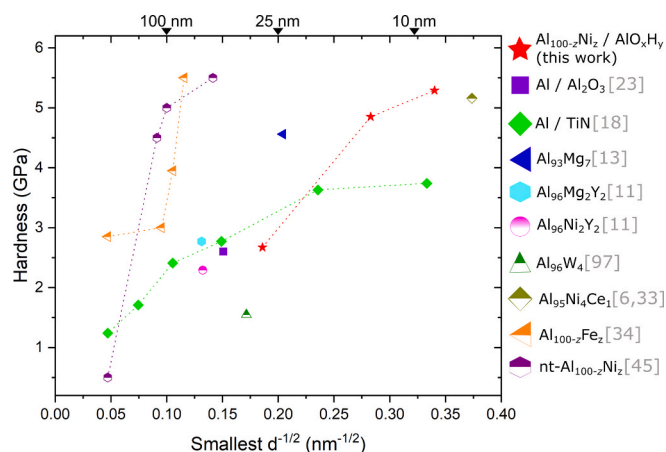


Fig. 10. Hardness of $\text{Al}_{100-z}\text{Ni}_z / \text{AlO}_x\text{H}_y$ thin films alongside high-performance nanocrystalline Al alloys. Where strength values are originally reported, the hardness was derived from the yield strength with a Taylor factor of 3: hardness $\sim 3 \times$ yield strength.

calculations identified significant strengthening through the formation of Al-Ni nanoclusters embedded in the refined FCC Al(–Ni) grains, competing with state-of-the-art high-performance nanocrystalline Al alloys.

In conclusion, these findings highlight the significant potential of dual-route-tailored, interface-engineered alloys synthesised via hybrid PVD / ALD beyond state-of-the-art nanocrystalline alloys, as exemplified by the $\text{Al}_{100-z}\text{Ni}_z / \text{AlO}_x\text{H}_y$ system investigated in this study. From a fundamental materials science perspective, this work unveils a novel approach to integrating previously uncombined artificial and spontaneously-precipitating microstructure control methods, paving the way for the design and deeper understanding of next-generation structural materials with enhanced performance and better controllability.

CRedit authorship contribution statement

Hendrik C. Jansen: Writing – review & editing, Writing – original draft, Methodology, Investigation, Conceptualization. **Amit Sharma:** Writing – review & editing, Investigation. **Marcus Hans:** Writing – review & editing, Investigation, Funding acquisition. **Jochen M Schneider:** Writing – review & editing, Resources, Funding acquisition. **Jakob Schwiedrzik:** Writing – review & editing, Supervision, Funding acquisition. **Johann Michler:** Writing – review & editing, Supervision, Resources, Funding acquisition, Conceptualization. **Thomas E.J. Edwards:** Writing – review & editing, Validation, Supervision, Methodology, Investigation, Funding acquisition, Conceptualization.

Declaration of competing interest

The authors declare that they have no known competing financial interests or personal relationships that could have appeared to influence the work reported in this paper.

Acknowledgements

HJC was supported by the Innosuisse Innovation project 109.352.1 “ORALCOAT”. TEJE gratefully acknowledges the support of Innosuisse (42220.1 IP-ENG) and JSPS KAKENHI Start-Up grant (24K23036). MH and JMS acknowledge funding from Deutsche Forschungsgemeinschaft (DFG) within the Collaborative Research Centre SFB 1394, “Structural and Chemical Atomic Complexity – From Defect Phase Diagrams to Materials Properties” (project ID 409476157). The authors emphasise support and assistance in this work by ScopeM ETHZ, especially by Dr. Joakim Reuteler.

Appendix A. Supplementary data

Supplementary data to this article can be found online at <https://doi.org/10.1016/j.matdes.2026.115580>.

Data availability

Data will be made available on request.

References

- [1] R.G. Guan, D. Tie, A review on grain refinement of aluminum alloys: Progresses, challenges and prospects, *Acta Metall. Sin. (Engl. Lett.)* 30 (2017) 409–432.
- [2] R. Chandel, N. Sharma, S.A. Bansal, A review on recent developments of aluminum-based hybrid composites for automotive applications, *Emergent Mater.* 4 (2021) 1243–1257.
- [3] M.A. Wahid, A.N. Siddiquee, Z.A. Khan, Aluminum alloys in marine construction: characteristics, application, and problems from a fabrication viewpoint, *Mar. Syst. Ocean Technol.* 15 (2020) 70–80.
- [4] A.Y. Ku, A.S. Khan, T. Gnäupel-Herold, Quasi-static and dynamic response, and texture evolution of two overaged Al 7056 alloy plates in T761 and T721 tempers: Experiments and modeling, *Int. J. Plast* 130 (2020).
- [5] C.J. Hung, S.K. Nayak, Y. Sun, C. Fennessy, V.K. Vedula, S. Tulyani, S.W. Lee, S. P. Alpay, R.J. Hebert, Novel Al-X alloys with improved hardness, *Mater. Des.* 192 (2020) 108699.
- [6] G.H. Balbus, J. Kappacher, D.J. Sprouster, F. Wang, J. Shin, Y.M. Eggeler, T. J. Rupert, J.R. Trelewicz, D. Kiener, V. Maier-Kiener, D.S. Gianola, Disordered interfaces enable high temperature thermal stability and strength in a nanocrystalline aluminum alloy, *Acta Mater.* 215 (2021) 116973.
- [7] K. Ma, H. Wen, T. Hu, T.D. Topping, D. Isheim, D.N. Seidman, E.J. Lavernia, J. M. Schoenung, Mechanical behavior and strengthening mechanisms in ultrafine grain precipitation-strengthened aluminum alloy, *Acta Mater.* 62 (2014) 141–155.
- [8] L. Fang, H.T. Xue, B. Zhang, Y. Kong, Y.C. Xin, W. Xu, X.Y. Li, Unlocking ultrahigh strength in dilute Al alloys: the synergy of stable grain boundary networks and solute clusters, *Acta Mater.* 286 (2025).
- [9] Z. Chen, F. Liu, H.F. Wang, W. Yang, G.C. Yang, Y.H. Zhou, A thermokinetic description for grain growth in nanocrystalline materials, *Acta Mater.* 57 (2009) 1466–1475.
- [10] J. Weissmüller, Alloy effects in nanostructures, *Nanostructured Mater.* 3 (1993) 261–272.
- [11] T. Lei, J. Shin, D.S. Gianola, T.J. Rupert, Bulk nanocrystalline Al alloys with hierarchical reinforcement structures via grain boundary segregation and complex formation, *Acta Mater.* 221 (2021) 117394.
- [12] H.A. Murdoch, C.A. Schuh, Estimation of grain boundary segregation enthalpy and its role in stable nanocrystalline alloy design, (2013).
- [13] S.C. Pun, W. Wang, A. Khalajhedayati, J.D. Schuler, J.R. Trelewicz, T.J. Rupert, Nanocrystalline Al-Mg with extreme strength due to grain boundary doping, *Mater. Sci. Eng. A* 696 (2017) 400–406.
- [14] W. Guo, Z. Pei, X. Sang, J.D. Poplawsky, S. Bruschi, J. Qu, D. Raabe, H. Bei, Shape-preserving machining produces gradient nanolaminate medium entropy alloys with high strain hardening capability, *Acta Mater.* 170 (2019) 176–186.
- [15] A. Misra, J.P. Hirth, R.G. Hoagland, Length-scale-dependent deformation mechanisms in incoherent metallic multilayered composites, *Acta Mater.* 53 (2005) 4817–4824.
- [16] J. Wang, A. Misra, An overview of interface-dominated deformation mechanisms in metallic multilayers, *Curr. Opin. Solid State Mater. Sci.* 15 (2011) 20–28.
- [17] L.J. Beyerlein, Z. Li, N.A. Mara, Mechanical Properties of Metal Nanolaminates, *Annu. Rev. Mater. Res.* 52 (2022) 281–304.
- [18] D. Bhattacharyya, N.A. Mara, R.G. Hoagland, A. Misra, Nanoindentation and microstructural studies of Al/TiN multilayers with unequal volume fractions, *Scr. Mater.* 58 (2008) 981–984.
- [19] S. Shen, H. Li, C. Wang, Y. Liang, N. Feng, N. Zhang, L. Yang, Mechanical properties and strengthening mechanism of Ni/Al nanolaminates: role of dislocation strengthening and constraint in soft layers, *Mater. Des.* 226 (2023) 111632.
- [20] W. Guo, E. Jägle, J. Yao, V. Maier, S. Korte-Kerzel, J.M. Schneider, D. Raabe, Intrinsic and extrinsic size effects in the deformation of amorphous CuZr/nanocrystalline Cu nanolaminates, *Acta Mater.* 80 (2014) 94–106.
- [21] B. Cheng, J.R. Trelewicz, Design of crystalline-amorphous nanolaminates using deformation mechanism maps, *Acta Mater.* 153 (2018) 314–326.
- [22] T.E.J. Edwards, T. Xie, N. Maria della Ventura, D. Casari, C. Guerra, E. Huszár, X. Maeder, J.J. Schwiedrzik, I. Utke, L. Pethö, J. Michler, On the thinnest Al₂O₃ interlayers in Al-based nanolaminates to enhance strength, and the role of constraint, *Acta Mater.* 240 (2022) 118345.
- [23] P. Baral, S. Jaddi, H. Wang, A. Orekhov, N. Gauquelin, A. Bagherpour, F. Van Loock, M. Coulombier, A. Favache, M. Rusinowicz, J. Verbeeck, S. Lucas, J. P. Raskin, H. Idrissi, T. Pardoën, Al₂O₃/Al hybrid nanolaminates with superior toughness, strength and ductility, *Nat. Commun.* 16 (2025) 1355.
- [24] K. Ming, Z. Zhu, W. Zhu, B. Fang, B. Wei, P.K. Liaw, X. Wei, J. Wang, S. Zheng, Enhancing strength and ductility via crystalline-amorphous nanoarchitectures in TiZr-based alloys, *Sci. Adv.* 8 (2022) 1–10.
- [25] B. Wei, W. Wu, D. Xie, M. Nastasi, J. Wang, Strength, plasticity, thermal stability and strain rate sensitivity of nanograined nickel with amorphous ceramic grain boundaries, *Acta Mater.* 212 (2021) 116918.
- [26] G. Li, J. Zhang, Y. Yang, Y. Wang, L. Wang, Y. Lu, J. Luan, G. Liu, J. Sun, Symbiotically engineered crystalline-amorphous nanostructure in a strong-yet-stable Al alloy with large twinning-induced plasticity, *Acta Mater.* 257 (2023) 119192.
- [27] T. Xie, T.E.J. Edwards, N.M. della Ventura, D. Casari, E. Huszár, L. Fu, L. Zhou, X. Maeder, J.J. Schwiedrzik, I. Utke, J. Michler, L. Pethö, Synthesis of model Al-Al₂O₃ multilayer systems with monolayer oxide thickness control by circumventing native oxidation, *Thin Solid Films* 711 (2020) 138287.
- [28] B. Putz, T.E.J. Edwards, E. Huszar, L. Pethö, P. Kreiml, M.J. Cordill, D. Thiaudiere, S. Chiroli, F. Zighem, D. Faurie, P.O. Renault, J. Michler, In situ fragmentation of Al/Al₂O₃ multilayers on flexible substrates in biaxial tension, *Mater. Des.* 232 (2023) 112081.
- [29] W. Dai, Q. Wang, K.H. Kim, S.H. Kwon, Al₂O₃/CrAlSiN multilayer coating deposited using hybrid magnetron sputtering and atomic layer deposition, *Ceram. Int.* 45 (2019) 11335–11341.
- [30] M. Wagih, P.M. Larsen, C.A. Schuh, Learning grain boundary segregation energy spectra in polycrystals, *Nat. Commun.* 11 (2020) 9.
- [31] P.R. Cantwell, M. Tang, S.J. Dillon, J. Luo, G.S. Rohrer, M.P. Harmer, Grain boundary complexions, *Acta Mater.* 62 (2014) 1–48.
- [32] J. Shin, F. Wang, G.H. Balbus, T. Lei, T.J. Rupert, D.S. Gianola, Optimizing thermal stability and mechanical behavior in segregation-engineered nanocrystalline Al–Ni–Ce alloys: a combinatorial study, *J. Mater. Res.* 37 (2022) 3083–3098.

- [33] G.H. Balbus, F. Wang, D.S. Gianola, Suppression of shear localization in nanocrystalline Al–Ni–Ce via segregation engineering, *Acta Mater.* 188 (2020) 63–78.
- [34] Q. Li, J. Wang, H. Wang, X. Zhang, Achieving strong and stable nanocrystalline Al alloys through compositional design, *J. Mater. Res.* 37 (2022) 183–207.
- [35] Y. Du, N. Clavaguera, Thermodynamic assessment of the Al–Ni system, *J. Alloys Compd.* 237 (1996) 20–32.
- [36] B. Cantor, R.W. Cahn, Metastable alloy phases by co-sputtering, *Acta Metall.* 24 (1976) 845–852.
- [37] D. Raabe, M. Herbig, S. Sandlöbes, Y. Li, D. Tytko, M. Kuzmina, D. Ponge, P. Choi, Grain boundary segregation engineering in metallic alloys: a pathway to the design of interfaces, *Curr. Opin. Solid State Mater. Sci.* 18 (2014) 253–261.
- [38] H.J.T. Ellingham, Reducibility of oxides and sulphides in metallurgical processes, *J. Soc. Chem. Ind.* 63 (1944).
- [39] C. Cancellieri, S. Gramatte, O. Politano, L. Lapeyre, F.F. Klimashin, K. Mackosz, I. Utke, Z. Novotny, A.M. Müller, C. Vockenhuber, V. Turlo, L.P.H. Jeurgens, Effect of hydrogen on the chemical state, stoichiometry and density of amorphous Al₂O₃ films grown by thermal atomic layer deposition, *Surf. Interface Anal.* 56 (2024) 293–304.
- [40] C. Guerra-Núñez, M. Döbeli, J. Michler, I. Utke, Reaction and growth Mechanisms in Al₂O₃ deposited via Atomic Layer Deposition: elucidating the Hydrogen Source, *Chem. Mater.* 29 (2017) 8690–8703.
- [41] H.C. Jansen, A. Sharma, K. Wiczerzak, G.K. Nayak, J.M. Schneider, J. Schwiedrzik, T.E.J. Edwards, J. Michler, On the efficacy of Xe + -pFIB preparation to avoid Ga + -FIB induced phase transformations in Al–Ni alloys, *Scr. Mater.* 260 (2025) 116589.
- [42] M. Klinger, More features, more tools, more CrysTBox, *J. Appl. Crystallogr.* 50 (2017) 1226–1234.
- [43] M. Hans, Z. Czizgany, D. Neuß, J.A. Sälker, H. Rueß, J. Krause, G.K. Nayak, D. Holec, J.M. Schneider, Probing the onset of wurtzite phase formation in (V,Al)N thin films by transmission electron microscopy and atom probe tomography, *Surf. Coatings Technol.* 442 (2022).
- [44] A.C. Fischer-Cripps, Critical review of analysis and interpretation of nanoindentation test data, *Surf. Coatings Technol.* 200 (2006) 4153–4165.
- [45] Y.F. Zhang, Q. Li, S.C. Xue, J. Ding, D.Y. Xie, J. Li, T. Niu, H. Wang, H. Wang, J. Wang, X. Zhang, Ultra-strong nanotwinned Al–Ni solid solution alloys with significant plasticity, *Nanoscale* 10 (2018) 22025–22034.
- [46] I. Petrov, P.B. Barna, L. Hultman, J.E. Greene, Microstructural evolution during film growth, *J. Vac. Sci. Technol. A Vacuum, Surfaces, Film.* 21 (2003) S117–S128.
- [47] A. Dulmaa, F.G. Coughon, R. Dedoncker, D. Depla, On the grain size-thickness correlation for thin films, *Acta Mater.* 212 (2021) 116896.
- [48] N. Cherkashin, A. Louiset, A. Chmielewski, D.J. Kim, C. Dubourdieu, S. Schamm-Chardon, Quantitative mapping of strain and displacement fields over HR-TEM and HR-STEM images of crystals with reference to a virtual lattice, *Ultramicroscopy* 253 (2023) 113778.
- [49] S. Shi, S. Qian, X. Hou, J. Mu, J. He, X. Chou, Structural and optical properties of amorphous Al₂O₃ thin film deposited by atomic layer deposition, *Adv. Condens. Matter Phys.* 2018 (2018).
- [50] A. Jain, S.P. Ong, G. Hautier, W. Chen, W.D. Richards, S. Dacek, S. Cholia, D. Gunter, D. Skinner, G. Ceder, K.A. Persson, Commentary: the materials project: a materials genome approach to accelerating materials innovation, *APL Mater.* 1 (2013).
- [51] S.P. Ong, L. Wang, B. Kang, G. Ceder, Li - Fe - P - O₂ phase diagram from first principles calculations, *Chem. Mater.* 20 (2008) 1798–1807.
- [52] L. Liliensten, B. Gault, New approach for FIB-preparation of atom probe specimens for aluminum alloys, *PLoS One* 15 (2020) 1–9.
- [53] J. Byloff, C.O.W. Trost, V. Devulapalli, S. Altat Husain, D. Faurie, P.O. Renault, T.E. J. Edwards, M.J. Cordill, D. Casari, B. Putz, Atomic layer-deposited interlayers for robust metal-polymer interfaces, *ACS Appl. Mater. Interfaces* (2025).
- [54] D.J. Larson, T.J. Prosa, R.M. Ulfig, B.P. Geiser, T.F. Kelly, *Atom Probe Tomography: A user's guide*, 2013.
- [55] S. Gramatte, V. Turlo, O. Politano, N. Jakse, C. Cancellieri, I. Utke, L.P.H. Jeurgens, Unveiling hydrogen chemical states in supersaturated amorphous alumina via machine learning-driven atomistic modeling, *npj Comput. Mater.* (2025) 1–13.
- [56] X. Zhou, A. Gupta, G.J. Tucker, G.B. Thompson, Manipulation of solute partitioning mechanisms for nanocrystalline stability, *Acta Mater.* 208 (2021) 116662.
- [57] B. Gault, A.J. Breen, Y. Chang, J. He, E.A. Jägle, P. Kontis, P. Kürsteiner, A. Kwiatkowski Da Silva, S.K. Makinen, I. Mouton, Z. Peng, D. Ponge, T. Schwarz, L.T. Stephenson, A. Szczepaniak, H. Zhao, D. Raabe, Interfaces and defect composition at the near-atomic scale through atom probe tomography investigations, *J. Mater. Res.* 33 (2018) 4018–4030.
- [58] H. Zhao, F. De Geuser, A. Kwiatkowski da Silva, A. Szczepaniak, B. Gault, D. Ponge, D. Raabe, Segregation assisted grain boundary precipitation in a model Al–Zn–Mg–Cu alloy, *Acta Mater.* 156 (2018) 318–329.
- [59] S. Ruan, K.L. Torres, G.B. Thompson, C.A. Schuh, Gallium-enhanced phase contrast in atom probe tomography of nanocrystalline and amorphous Al–Mn alloys, *Ultramicroscopy* 111 (2011) 1062–1072.
- [60] H. Aboulfadl, J. Deges, P. Choi, D. Raabe, Dynamic strain aging studied at the atomic scale, *Acta Mater.* 86 (2015) 34–42.
- [61] B. Yang, Q. He, H. Wang, C. Wang, F. Guo, R. Hu, C. Wang, G. Fan, Q. Wang, W. Cao, C. Huang, Achieving an extra-high-strength yet ductile steel by synergistic effects of TRIP and maraging, *Mater. Res. Lett.* 11 (2023) 578–585.
- [62] F. De Geuser, B. Gault, Metrology of small particles and solute clusters by atom probe tomography, *Acta Mater.* 188 (2020) 406–415.
- [63] S. Jiang, Y. Xu, R. Wang, X. Chen, C. Guan, Y. Peng, F. Liu, M. Wang, X. Liu, S. Zhang, G. Tian, S. Jin, H. Wang, H. Toda, X. Jin, G. Liu, B. Gault, J. Sun, Structurally complex phase engineering enables hydrogen-tolerant Al alloys, *Nature* 641 (2025).
- [64] W. Xu, L.P. Dávila, Tensile nanomechanics and the Hall-Petch effect in nanocrystalline aluminium, *Mater. Sci. Eng. A* 710 (2018) 413–418.
- [65] N. Kamikawa, X. Huang, N. Tsuji, N. Hansen, Strengthening mechanisms in nanostructured high-purity aluminium deformed to high strain and annealed, *Acta Mater.* 57 (2009) 4198–4208.
- [66] E. Orowan, Dislocations in Metals, *Amer. Inst. Min. Engrs*, 1954.
- [67] G.S. Ansell, F.V. Lenel, Criteria for yielding of dispersion-strengthened alloys, *Acta Metall.* 8 (1960) 612–616.
- [68] R. Labusch, A Statistical theory of solid solution hardening, *Phys. Status Solidi* 41 (1970) 659–669.
- [69] R. Labusch, Statistical theories of solid solution hardening, *Acta Metall.* 20 (1972) 917–927.
- [70] J.Y. Zhang, Y. Liu, J. Chen, Y. Chen, G. Liu, X. Zhang, J. Sun, Mechanical properties of crystalline Cu/Zr and crystal-amorphous Cu/Cu–Zr multilayers, *Mater. Sci. Eng. A* 552 (2012) 392–398.
- [71] Y. Cui, O.T. Abad, F. Wang, P. Huang, T.J. Lu, K.W. Xu, J. Wang, Plastic deformation modes of CuZr/Cu Multilayers, *Sci. Rep.* 6 (2016) 2–7.
- [72] B. Cheng, J.R. Trelewicz, Mechanistic coupling of dislocation and shear transformation zone plasticity in crystalline-amorphous nanolaminates, *Acta Mater.* 117 (2016) 293–305.
- [73] Y. Wang, J. Li, A.V. Hamza, T.W. Barbee, Ductile crystalline-amorphous nanolaminates, *Proc. Natl. Acad. Sci. U. S. A.* 104 (2007) 11155–11160.
- [74] O. Glushko, M. Mühlbacher, C. Gammer, M.J. Cordill, C. Mitterer, J. Eckert, Exceptional fracture resistance of ultrathin metallic glass films due to an intrinsic size effect, *Sci. Rep.* 9 (2019) 1–9.
- [75] Y.Y. Xiao, X.F. Kong, B.N. Yao, D. Legut, T.C. Germann, R.F. Zhang, Acta Materialia Atomistic insight into the dislocation nucleation at crystalline / crystalline and crystalline / amorphous interfaces without full symmetry, *Acta Mater.* 162 (2019) 255–267.
- [76] Q. Xu, M. Liang, G. Lyu, J. Qiao, C. Wei, W. Huo, Nucleation mechanisms of shear bands in amorphous alumina, *Mater. Chem. Phys.* 325 (2024) 129783.
- [77] S. Huang, I.J. Beyerlein, C. Zhou, Nanograin size effects on the strength of biphasic nanolayered composites, *Sci. Rep.* 7 (2017) 1–10.
- [78] D. Shi, B. Wen, R. Melnik, S. Yao, T. Li, First-principles studies of Al–Ni intermetallic compounds, *J. Solid State Chem.* 182 (2009) 2664–2669.
- [79] R.C. Cammarata, Surface and interface stress effects in thin films, *Prog. Surf. Sci.* 46 (1994) 1–38.
- [80] H.T. Li, L.F. Chen, X. Yuan, W.Q. Zhang, J.R. Smith, A.G. Evans, Interfacial stoichiometry and adhesion at metal/ α -Al₂O₃ interfaces, *J. Am. Ceram. Soc.* 94 (2011) s154–s159.
- [81] J.M. Schneider, K. Larsson, J. Lu, E. Olsson, B. Hjörvarsson, Role of hydrogen for the elastic properties of alumina thin films, *Appl. Phys. Lett.* 80 (2002) 1144–1146.
- [82] L. Nicola, E. Van Der Giessen, A. Needleman, Size effects in polycrystalline thin films analyzed by discrete dislocation plasticity, *Thin Solid Films* 479 (2005) 329–338.
- [83] M.Y. Tong, C.K.C. Lieou, I.J. Beyerlein, Deformation profile and interface-mediated defect interaction in Cu / CuZr nanolaminates : an effective-temperature description, *Phys. Rev. Mater.* 073602 (2019) 1–12.
- [84] B. Ding, J. Du, J. Wang, Interface shearing promoted plastic flow instability of nanolaminated composites, *Int. J. Mech. Sci.* 270 (2024) 109114.
- [85] M.M. Shahzamanian, S.S. Akhtar, A.F.M. Arif, W.J. Basirun, K.S. Al-Athel, M. Schneider, N. Shakelly, A.S. Hakeem, A.A. Abubakar, P.D. Wu, Thermo-mechanical properties prediction of Ni-reinforced Al₂O₃ composites using micro-mechanics based representative volume elements, *Sci. Rep.* 12 (2022) 1–24.
- [86] G.K. Williamson, R.E. Smallman III, Dislocation densities in some annealed and cold-worked metals from measurements on the X-ray Debye-Scherrer spectrum, *Philos. Mag.* 1 (1956) 34–46.
- [87] A. Kelly, R. Nicholson, Dislocation-Particle Interactions, in: *Strength. Methods Cryst.*, Amsterdam, New York, Elsevier Pub. Co., 1971: p. 627.
- [88] R. Santos-Güemes, B. Bellón, G. Esteban-Manzanares, J. Segurado, L. Capolungo, J. Llorca, Multiscale modelling of precipitation hardening in Al–Cu alloys: Dislocation dynamics simulations and experimental validation, *Acta Mater.* 188 (2020) 475–485.
- [89] H. Van Swygenhoven, P.M. Derlet, A.G. Frøseth, Nucleation and propagation of dislocations in nanocrystalline fcc metals, *Acta Mater.* 54 (2006) 1975–1983.
- [90] G. Esteban-Manzanares, B. Bellón, E. Martínez, I. Papadimitriou, J. Llorca, Strengthening of Al–Cu alloys by Guinier–Preston zones: Predictions from atomistic simulations, *J. Mech. Phys. Solids* 132 (2019) 103675.
- [91] Y. Hu, W.A. Curtin, Modeling peak-aged precipitate strengthening in Al–Mg–Si alloys, *J. Mech. Phys. Solids* 151 (2021).
- [92] M. Rajagopalan, K. Darling, S. Turnage, R.K. Koju, B. Hornbuckle, Y. Mishin, K. N. Solanki, Microstructural evolution in a nanocrystalline Cu–Ta alloy: a combined in-situ TEM and atomistic study, *Mater. Des.* 113 (2017) 178–185.
- [93] K.A. Darling, M. Rajagopalan, M. Komarasamy, M.A. Bhatia, B.C. Hornbuckle, R. S. Mishra, K.N. Solanki, Extreme creep resistance in a microstructurally stable nanocrystalline alloy, *Nature* 537 (2016) 378–381.
- [94] C. Kale, S. Turnage, P. Garg, I. Adlakha, S. Srinivasan, B.C. Hornbuckle, K. Darling, K.N. Solanki, Thermo-mechanical strengthening mechanisms in a stable nanocrystalline binary alloy – a combined experimental and modeling study, *Mater. Des.* 163 (2019) 107551.

- [95] J. Wang, Q. Zhou, S. Shao, A. Misra, Strength and plasticity of nanolaminated materials, 3831 (2017).
- [96] J.Y. Zhang, S. Lei, Y. Liu, J.J. Niu, Y. Chen, G. Liu, X. Zhang, J. Sun, Length scale-dependent deformation behavior of nanolayered Cu / Zr micropillars, *Acta Mater.* 60 (2012) 1610–1622.
- [97] K.V. Rajulapati, R.O. Scattergood, K.L. Murty, Z. Horita, T.G. Langdon, C.C. Koch, Mechanical properties of bulk nanocrystalline aluminum-tungsten alloys, *Metall. Mater. Trans. A Phys. Metall. Mater. Sci.* 39 (2008) 2528–2534.